

¹ **Searches for Supersymmetry using the α_T**
² **variable with the CMS detector at the LHC**

³ Darren Burton

⁴ Imperial College London
⁵ Department of Physics

⁶ A thesis submitted to Imperial College London
⁷ for the degree of Doctor of Philosophy

Abstract

10

Declaration

11

I, the author of this thesis, declare that the work presented within this
document to be my own. The work presented in Chapters 3.4.1, 4 and 5
is a result of the authors own work or that of which I have been a major
contributor unless explicitly stated otherwise, and is carried out within the
context of the Imperial College London and CERN SUSY groups, itself a
subsection of the greater CMS collaboration. All figures and studies taken
from external sources are referenced appropriately throughout this document.

18

Darren Burton

19

Acknowledgements

20

Of the many people who deserve thanks, some are particularly prominent....

Preface

Contents

23	List of Figures	viii
24	List of Tables	xii
25	1. Introduction	2
26	2. A Theoretical Overview	5
27	2.1. The Standard Model	5
28	2.1.1. Gauge Symmetries of the SM	7
29	2.1.2. The Electroweak Sector and Electroweak Symmetry Breaking	9
30	2.2. Motivation for Physics Beyond the Standard Model	13
31	2.3. Supersymmetry Overview	15
32	2.3.1. R-Parity	16
33	2.4. Experimental signatures of SUSY at the LHC	17
34	2.4.1. Simplified Models	18
35	3. The LHC and the CMS Detector	20
36	3.1. The LHC	20
37	3.2. The CMS detector	23
38	3.2.1. Detector Subsystems	23
39	3.2.2. Tracker	24
40	3.2.3. Electromagnetic Calorimeter	25
41	3.2.4. Hadronic Calorimeter	26
42	3.2.5. Muon Systems	27
43	3.3. Event Reconstruction and Object Definition	28
44	3.3.1. Jets	28
45	3.3.2. B-tagging	30
46	3.4. Triggering System	32
47	3.4.1. The Level-1 Trigger	34

48	3.4.2. L1 Trigger Jet Algorithm	35
49	3.4.3. Measuring L1 Jet Trigger Efficiencies	36
50	3.4.4. Effects of the L1 Jet Seed	38
51	3.4.5. Robustness of L1 Jet Performance against Pile-up	41
52	3.4.6. Summary	43
53	4. SUSY searches in Hadronic Final States	45
54	4.1. An introduction to the α_T search	46
55	4.1.1. The α_T variable	48
56	4.2. Search Strategy	50
57	4.2.1. Physics Objects	53
58	4.2.2. Event Selection	53
59	4.2.3. Control Sample Definition	53
60	4.3. Trigger Strategy	56
61	4.4. A method to determine MC yields with higher statistical precision	56
62	4.5. Systematic Uncertainties on Transfer Factors	56
63	4.6. Searches for Natural SUSY with B-tag templates.	56
64	5. Results	57
65	5.1. Statistical Interpretation	57
66	5.2. Interpretation in Simplified Signal Models	57
67	A. Miscellaneous	58
68	A.1. Noise Filters	58
69	A.2. Primary Vertices	59
70	B. L1 Jets	60
71	B.1. Jet matching efficiencies	60
72	B.2. Leading Jet Energy Resolution	61
73	B.3. Resolution for Energy Sum Quantities	64
74	Bibliography	70

⁷⁵ List of Figures

⁷⁶ 2.1.	One loop quantum corrections to the Higgs squared mass parameter m_h^2 due to a fermion.	⁷⁷ 14
⁷⁸ 2.2.	Two example simplified model decay chains.	⁷⁹ 19
⁸⁰ 3.1.	A top down layout of the LHC, with the position of the four main detectors labelled.	⁸¹ 21
⁸² 3.2.	The total integrated luminosity delivered to and collected by Compact Muon Solenoid (CMS) during the 2012 8 TeV pp runs	⁸³ 22
⁸³ 3.3.	A pictorial depiction of the CMS detector.	⁸⁴ 24
⁸⁴ 3.4.	Illustration of the CMS Electromagnetic CALorimeter (ECAL).	⁸⁵ 26
⁸⁵ 3.5.	Schematic of the CMS Hadronic CALorimeter (HCAL).	⁸⁶ 27
⁸⁶ 3.6.	Combined Secondary Vertex (CSV) algorithm discriminator values in enriched $t\bar{t}$ and inclusive multi jet samples	⁸⁷ 31
⁸⁸ 3.7.	Data/MC b-tag scale factors derived using the Combined Secondary Vertex Medium Working Point (CSVM) tagger.	⁸⁹ 32
⁹⁰ 3.8.	Data/MC mis-tag scale factors derived using the CSVM tagger.	⁹¹ 33
⁹¹ 3.9.	The CMS Level 1 Trigger (L1) Trigger system.	⁹² 34
⁹² 3.10.	Illustration of the Level-1 jet finding algorithm.	⁹³ 36
⁹³ 3.11.	L1 jet efficiency turn-on curves as a function of the offline CaloJet and PFJet E_T	⁹⁴ 38
⁹⁵ 3.12.	L1 jet efficiency turn-on curves as a function of the offline CaloJet E_T for the 2012 run period B and C.	⁹⁶ 39

97	3.13. Trigger cross section for the L1HTT150 trigger path.	40
98	3.14. L1 H_T efficiency turn-on curves as a function of the offline CaloJet H_T	41
99	3.15. L1 jet efficiency turn-on curves as a function of the leading offline E_T Calo	
100	(left) and PF (right) jet, for low, medium and high pile-up conditions.	42
101	3.16. Fit values from an Exponentially Modified Gaussian (EMG) function fitted	
102	to the resolution plots of leading Calo jet E_T measured as a function of	
103	$\frac{(L1\ E_T - \text{Offline}\ E_T)}{\text{Offline}\ E_T}$ for low, medium and high pile-up conditions.	43
104	3.17. Fit values from an EMG function fitted to the resolution plots of leading	
105	PF jet E_T measured as a function of $\frac{(L1\ E_T - \text{Offline}\ E_T)}{\text{Offline}\ E_T}$ for low, medium and	
106	high pile-up conditions.	44
107	4.1. Reconstructed offline H_T for 11.7fb^{-1} of data after a basic pre-selection.	48
108	4.2. The event topologies of background QCD dijet events (right) and a generic	
109	SUPERSYmmetry (SUSY) signature with genuine \cancel{E}_T (left).	48
110	4.3. The α_T distributions for the low 2-3 (left) and high ≥ 4 (right) jet	
111	multiplicities after a full analysis selection and shown for $H_T > 375$	50
112	4.4. Pictorial depiction of the analysis strategy employed by the α_T search to	
113	increase sensitivity to a wide spectra of SUSY models.	52
114	B.1. Leading jet matching efficiency as a function of the offline CaloJet E_T	60
115	B.2. Resolution plots of the leading offline Calo E_T measured as a function of	
116	$\frac{(L1\ E_T - \text{Offline}\ E_T)}{\text{Offline}\ E_T}$ for low (a), medium (b) and high (c) pile-up conditions.	62
117	B.3. Resolution plots of the leading off-line PF E_T measured as a function of	
118	$\frac{(L1\ E_T - \text{Offline}\ E_T)}{\text{Offline}\ E_T}$ for low (a), medium (b) and high (c) pile-up conditions.	64
119	B.4. $\sum E_T$ resolution parameters in bins of Calo $\sum E_T$ measured for the defined	
120	low, medium and high pile up conditions.	65
121	B.5. $\sum E_T$ resolution parameters in bins of PF $\sum E_T$ measured for the defined	
122	low, medium and high pile up conditions.	65
123	B.6. \cancel{E}_T resolution parameters in bins of Calo \cancel{E}_T measured for the defined	
124	low, medium and high pile up conditions.	66

125	B.7. \cancel{E}_T resolution parameters in bins of PF \cancel{E}_T measured for the defined low,	
126	medium and high pile up conditions.	66
127	B.8. H_T resolution parameters in bins of Calo H_T measured for the defined	
128	low, medium and high pile up conditions.	67
129	B.9. H_T resolution parameters in bins of PF H_T measured for the defined low,	
130	medium and high pile up conditions.	67
131	B.10. \cancel{H}_T resolution parameters in bins of \cancel{H}_T measured for the defined low,	
132	medium and high pile up conditions.	68
133	B.11. \cancel{H}_T resolution parameters in bins of PF \cancel{H}_T measured for the defined low,	
134	medium and high pile up conditions.	68

¹³⁵ List of Tables

¹³⁶	2.1. The fundamental particles of the Standard Model (SM), with spin, charge and mass displayed.	6
¹³⁷		
¹³⁸	3.1. Results of a cumulative EMG function fit to the turn-on curves for L1 single jet triggers in 2012 Run Period C.	38
¹³⁹		
¹⁴⁰	3.2. Results of a cumulative EMG function fit to the turn-on curves for L1 single jet triggers in the 2012 run period B and C.	39
¹⁴¹		
¹⁴²	3.3. Results of a cumulative EMG function fit to the turn-on curves for H_T in 2012 run period B and C.	40
¹⁴³		
¹⁴⁴	3.4. Results of a cumulative EMG function fit to the efficiency turn-on curves for L1 single jet triggers in the 2012 run period C, for low,medium and high pile-up conditions.	41
¹⁴⁵		
¹⁴⁶		
¹⁴⁷	3.5. Results of a cumulative EMG function fit to the efficiency turn-on curves for Level-1 single jet triggers in the 2012 run period C, for low,medium and high pile-up conditions.	42
¹⁴⁸		
¹⁴⁹		
¹⁵⁰	4.1. A summary of the Simplified Model Spectra (SMS) models interpreted in this analysis, involving both direct (D) and gluino-induced (G) production of squarks and their decays.	46
¹⁵¹		
¹⁵²		
¹⁵³	4.2. Muon Id.	53
¹⁵⁴		
¹⁵⁵	4.3. Muon Id.	53
¹⁵⁶		
¹⁵⁷	B.1. Results of a cumulative EMG function fit to the turn-on curves for the matching efficiency of the leading jet in an event to a Level-1 jet in run 2012C and 2012B data.	61

“The Universe is about 1,000,000 years old.”

— Matthew Kenzie, 1987-present : Discoverer of the Higgs Boson.

Chapter 1.

¹⁶⁰ Introduction

¹⁶¹ During the 20th century great advances have been made in our understanding of the
¹⁶² universe, where it comes from, where it is going and what it is made of. The Standard
¹⁶³ Model (**SM**) first formulated in the 1960's is one of the crowning achievements in science's
¹⁶⁴ quest to explain the most fundamental processes and interactions that make up our
¹⁶⁵ universe. It has provided a highly successful explanation of a wide range of phenomena
¹⁶⁶ in Particle Physics and has stood up to extensive experimental scrutiny [1].

¹⁶⁷ Despite it's successes it is not a complete theory, with significant questions remaining
¹⁶⁸ unanswered. It describes only three of the four known forces with gravity not incorpo-
¹⁶⁹ rated within the framework of the **SM**. Cosmological experiments infer that just $\sim 4\%$
¹⁷⁰ of the observable universe exists as matter, with elusive "Dark Matter" accounting for a
¹⁷¹ further $\sim 23\%$ [2]. However no particle predicted by the **SM** is able to account for it. At
¹⁷² higher energy scales and small distances the (non-)unification of the fundamental forces
¹⁷³ point to problems with the **SM** at least at higher energies not yet probed experimentally.

¹⁷⁴ Many theories exist as extensions to the **SM** and predict a range of observables
¹⁷⁵ that can be detected at the Large Hadron Collider (**LHC**) of which SUperSYmmetry
¹⁷⁶ (**SUSY**) is one such example. It predicts a new symmetry of nature in which all current
¹⁷⁷ particles in the **SM** would have a corresponding supersymmetric partner. Common to
¹⁷⁸ most Supersymmetric theories is a stable, weakly interacting Lightest Supersymmetric
¹⁷⁹ Partner (**LSP**), which has the properties of a possible dark matter candidate. The **SM**
¹⁸⁰ and the main principles of Supersymmetric theories are outlined in Chapter 2, with
¹⁸¹ emphasis placed on how experimental signatures of **SUSY** may reveal themselves at
¹⁸² the **LHC**.

183 The experimental goal of the LHC is to further test the framework of the SM,
184 exploring the TeV mass scale for the first time, and to seek a connection between the
185 particles produced in proton collisions and dark matter. The first new discovery by
186 this extraordinary machine was announced on the 4th of July 2012. The long-awaited
187 discovery was the culmination decades of experimental endeavours in the search for the
188 Higgs boson, providing an answer to the mechanism of electroweak symmetry breaking
189 within the SM [3][4].

190 This discovery was made possible through data taken by the two multi purpose
191 detectors (CMS and A Toroidal LHC Apparatus (ATLAS)) located on the LHC ring.
192 An experimental description of the CMS detector and the LHC is described in Chapter 3,
193 including some of the object reconstruction used by CMS in searches for SUSY signatures.
194 The performance of the CMS Level-1 calorimeter trigger, benchmarked by the author is
195 also included within this chapter.

196 The analysis conducted by the author is detailed within Chapter 4. This chapter
197 contains a description of the search for evidence of the production of Supersymmetric
198 particles at the LHC. The main basis of the search centres around the kinematic
199 dimensionless α_T variable, which provides strong rejection of backgrounds with fake
200 missing energy signatures whilst maintaining good sensitivity to a variety of SUSY
201 topologies. The author's work as an integral part of the analysis group is documented in
202 detail, which has culminated in numerous publications over the past two years. The latest
203 of which was published in the European Physical Journal C (EPJC) [5] and contains the
204 results which are discussed within this and the sequential Chapter.

205 The author in particular has played a major role in the extension of the α_T analysis into
206 the additional b-tagged and jet multiplicity dimensions increasing the sensitivity of the
207 analysis to a range of SUSY topologies. Additionally the author has worked extensively
208 in both increasing the statistical precision of electroweak predictions measured from
209 simulation through analytical techniques, and the derivation of a data driven systematic
210 uncertainty through the establishment of closure tests within the control samples of the
211 analysis.

212 Also included within this Chapter is a method to search for SUSY signatures which
213 are rich in top and bottom flavoured jet final states. A parametrisation of the b-tagging
214 distribution for different Electroweak processes is used to establish templates, which
215 are then used to estimate the expected number of 3 or 4 b-tagged jet events from SM

216 processes. The α_T search is used as a cross check for this template method to establish
217 it's functionality.

218 Finally the interpretation of such results within the framework of a variety of Simplified
219 Model Spectra (**SMS**), which describe an array of possible **SUSY** event topologies is
220 documented in Chapter 5. A description of the statistical model used to derive these
221 interpretations and the possible implications of the results presented in this thesis is
222 discussed within this Chapter. Natural units are used throughout this thesis in which \hbar
223 = c = 1.

Chapter 2.

²²⁴ A Theoretical Overview

²²⁵ Within this chapter, a brief introduction and background to the **SM** is given. Its success
²²⁶ as a rigorously tested and widely accepted theory is discussed as well as the deficiencies
²²⁷ with this theory that hint there this theory is not a complete description of our universe.
²²⁸ The motivations for new physics at the TeV scale and in particular Supersymmetric
²²⁹ theories are outlined within Section (2.3), with the chapter concluding with how an
²³⁰ experimental signature of such theories can be produced and observed at the **LHC**,
²³¹ Section (2.4).

²³² 2.1. The Standard Model

²³³ The **SM** is the name given to the relativistic Quantum Field Theory (**QFT**), where
²³⁴ particles are represented as excitations of fields, which describes the interactions and
²³⁵ properties of all the known elementary particles [6][7][8][9]. It is a renormalisable field
²³⁶ theory which contains three symmetries: $SU(3)$ for colour charge, $SU(2)$ for weak isospin
²³⁷ and $U(1)$ relating to weak hyper charge, which require its Lagrangian \mathcal{L}_{SM} to be invariant
²³⁸ under local gauge transformation.

²³⁹ Within the **SM** theory, matter is composed of spin $\frac{1}{2}$ fermions, which interact with each
²⁴⁰ other via the exchange of spin-1 gauge bosons. A summary of the known fundamental
²⁴¹ fermions and bosons is given in Table 2.1.

²⁴² Fermions are separated into quarks and leptons of which only quarks interact with
²⁴³ the strong nuclear force. Quarks unlike leptons are not seen as free particles in nature,
²⁴⁴ but rather exist only within baryons, composed of three quarks with an overall integer

Particle	Symbol	Spin	Charge	Mass (GeV)
First Generation Fermions				
Electron Neutrino	ν_e	$\frac{1}{2}$	0	$< 2.2 \times 10^{-6}$
Electron	e	$\frac{1}{2}$	-1	0.51×10^{-3}
Up Quark	u	$\frac{1}{2}$	$\frac{2}{3}$	$2.3^{+0.7}_{-0.5} \times 10^{-3}$
Down Quark	d	$\frac{1}{2}$	$-\frac{1}{3}$	$4.8^{+0.7}_{-0.3} \times 10^{-3}$
Second Generation Fermions				
Muon Neutrino	ν_μ	$\frac{1}{2}$	0	-
Muon	μ	$\frac{1}{2}$	-1	1.05×10^{-3}
Charm Quark	c	$\frac{1}{2}$	$\frac{2}{3}$	1.275 ± 0.025
Strange Quark	s	$\frac{1}{2}$	$-\frac{1}{3}$	$95 \pm 5 \times 10^{-3}$
Third Generation Fermions				
Tau Neutrino	ν_τ	$\frac{1}{2}$	0	-
Tau	τ	$\frac{1}{2}$	-1	1.77
Top Quark	t	$\frac{1}{2}$	$\frac{2}{3}$	173.5 ± 0.8
Bottom Quark	b	$\frac{1}{2}$	$-\frac{1}{3}$	4.65 ± 0.03
Gauge Bosons				
Photon	γ	1	0	0
W Boson	W^\pm	1	± 1	80.385 ± 0.015
Z Boson	Z	1	0	91.187 ± 0.002
Gluons	g	1	0	0
Higgs Boson	H	0	0	125.3 ± 0.5 [4]

Table 2.1.: The fundamental particles of the SM, with spin, charge and mass displayed. Latest mass measurements taken from [1].

charge, and quark-anti-quark pairs called mesons. Both leptons and quarks are grouped into three generations which have the same properties, but with ascending mass in each subsequent generation.

The gauge bosons mediate the interactions between fermions. The field theories of Quantum Electro-Dynamics (QED) and Quantum Chromo-Dynamics (QCD), yield massless mediator bosons, the photon and eight coloured gluons which are consequences of the gauge invariance of those theories, detailed in Section (2.1.1).

The unification of the electromagnetic and weak-nuclear forces into the current Electroweak theory yield the weak gauge bosons, W^\pm and Z through the mixing of the associated gauge fields. The force carriers of this theory were experimentally detected by

255 the observation of weak neutral current, discovered in 1973 in the Gargamelle bubble
 256 chamber located at European Organization for Nuclear Research (**CERN**) [10], with the
 257 masses of and the weak gauge bosons measured by the UA1 and U2 experiments at the
 258 Super Proton Synchrotron (**SPS**) collider in 1983 [11][12].

259 2.1.1. Gauge Symmetries of the SM

260 Symmetries are of fundamental importance in the description of physical phenomena.
 261 Noether's theorem states that for a dynamical system, the consequence of any symmetry
 262 is an associated conserved quantity [13]. Invariance under translations, rotations, and
 263 Lorentz transformations in physical systems lead to conservation of momentum, energy
 264 and angular momentum.

265 In the **SM**, a quantum theory described by Lagrangian formalism, the weak, strong and
 266 electromagnetic interactions are described in terms of “gauge theories”. A gauge theory
 267 possesses invariance under a set of “local transformations”, which are transformations
 268 whose parameters are space-time dependent. The requirement of gauge invariance within
 269 the **SM** necessitates the introduction of force-mediating gauge bosons and interactions
 270 between fermions and the bosons themselves. Given the nature of the topics covered by
 271 this thesis, the formulation of Electroweak Sector (**EWK**) within the **SM** Lagrangian is
 272 reviewed within this section.

273 The simplest example of the application of the principle of local gauge invariance
 274 within the **SM** is in Quantum Electro-Dynamics (**QED**), the consequences of which
 275 require a massless photon field [14][15].

276 Starting from the free Dirac Lagrangian written as

$$\mathcal{L} = \bar{\psi}(i\gamma^\mu \partial_\mu - m)\psi, \quad (2.1)$$

277 where ψ represents a free non interacting fermionic field, with the matrices $\gamma^\mu, \mu \in$
 278 $0, 1, 2, 3$ defined by the anti commutator relationship $\gamma^\mu \gamma^\nu + \gamma^\nu \gamma^\mu = 2\eta^{\mu\nu} I_4$ where $\eta^{\mu\nu}$ is
 279 the flat space-time metric $(+, -, -, -)$ and I_4 is the 4×4 identity matrix.

280 Under a local U(1) abelian gauge transformation in which ψ transforms as:

$$\psi(x) \rightarrow \psi'(x) = e^{i\theta(x)}\psi(x) \quad \bar{\psi}(x) \rightarrow \bar{\psi}'(x) = e^{i\theta(x)}\bar{\psi}(x) \quad (2.2)$$

281 the kinetic term of the Lagrangian does not remain invariant, due to the partial
282 derivative interposed between the $\bar{\psi}$ and ψ yielding,

$$\partial_\mu \psi \rightarrow e^{i\theta(x)} \partial_\mu \psi + i e^{i\theta(x)} \psi \partial_\mu \theta. \quad (2.3)$$

283 To ensure that \mathcal{L} remains invariant, a modified derivative, D_μ , that transforms
284 covariantly under phase transformations is introduced. In doing this a vector field A_μ
285 with transformation properties that cancel out the unwanted term in (2.3) must also be
286 included,

$$D_\mu \equiv \partial_\mu - ieA_\mu, \quad A_\mu \rightarrow A_\mu + \frac{1}{e} \partial_\mu \theta. \quad (2.4)$$

287 Invariance of the Lagrangian is then achieved by replacing ∂_μ by D_μ :

$$\begin{aligned} \mathcal{L} &= i\bar{\psi}\gamma^\mu D_\mu \psi - m\bar{\psi}\psi \\ &= \bar{\psi}(i\gamma^\mu \partial_\mu - m)\psi + e\bar{\psi}\gamma^\mu \psi A_\mu \end{aligned} \quad (2.5)$$

288 An additional interaction term is now present in the Lagrangian, coupling the Dirac
289 particle to this vector field, which is interpreted as the photon in QED. To regard this
290 new field as the physical photon field, a term corresponding to its kinetic energy must be
291 added to the Lagrangian from Equation (2.5). Since this term must also be invariant
292 under the conditions of Equation (2.4), it is defined in the form $F_{\mu\nu} = \partial^\mu A^\nu - \partial^\nu A^\mu$.

293 This then leads to the Lagrangian of QED:

$$\mathcal{L}_{QED} = \underbrace{i\bar{\psi}\gamma^\mu\partial_\mu\psi - \frac{1}{4}F_{\mu\nu}F^{\mu\nu}}_{\text{kinetic term}} + \underbrace{m\bar{\psi}\psi}_{\text{mass term}} + \underbrace{e\bar{\psi}\gamma^\mu\psi A_\mu}_{\text{interaction term}} \quad (2.6)$$

Within the Lagrangian there remains no mass term of the form $m^2A_\mu A^\mu$, which is prohibited by gauge invariance. This implies that the gauge particle, the photon, must be massless.

2.1.2. The Electroweak Sector and Electroweak Symmetry Breaking

The same application of gauge symmetry and the requirement of local gauge invariance can be used to unify QED and the Weak force in the Electroweak Sector (EWK). The nature of EWK interactions is encompassed within a Lagrangian invariant under transformations of the group $SU(2)_L \times U(1)_Y$.

The weak interactions from experimental observation [16], are known to violate parity and are therefore not symmetric under interchange of left and right helicity fermions. Thus within the SM the left and right handed parts of these fermion fields are treated separately. A fermion field is then split into two left and right handed chiral components, $\psi = \psi_L + \psi_R$, where $\psi_{L/R} = (1 \pm \gamma^5)\psi$.

The $SU(2)_L$ group is the special unitary group of 2×2 matrices U satisfying $UU^\dagger = I$ and $\det(U) = 1$. It may be written in the form $U = e^{-i\omega_i T_i}$, with the generators of the group $T_i = \frac{1}{2}\tau_i$ where τ_i , $i \in 1,2,3$ being the 2×2 Pauli matrices

$$\tau_1 = \begin{pmatrix} 0 & 1 \\ 1 & 0 \end{pmatrix} \quad \tau_2 = \begin{pmatrix} 0 & -i \\ i & 0 \end{pmatrix} \quad \tau_3 = \begin{pmatrix} 1 & 0 \\ 0 & -1 \end{pmatrix}, \quad (2.7)$$

which form a non Abelian group obeying the commutation relation $[T^a, T^b] \equiv if^{abc}T^c \neq 0$. The gauge fields that accompany this group are represented by $\hat{W}_\mu = (\hat{W}_\mu^1, \hat{W}_\mu^2, \hat{W}_\mu^3)$ and act only on the left handed component of the fermion field ψ_L .

³¹⁴ One additional generator Y which represents the hypercharge of the particle under
³¹⁵ consideration is introduced through the $U(1)_Y$ group acting on both components of the
³¹⁶ fermion field, with an associated vector boson field \hat{B}_μ .

³¹⁷ The $SU(2)_L \times U(1)_Y$ transformations of the left and right handed components of ψ
³¹⁸ are summarised by,

$$\begin{aligned}\chi_L &\rightarrow \chi'_L = e^{i\theta(x) \cdot T + i\theta(x)Y} \chi_L, \\ \psi_R &\rightarrow \psi'_R = e^{i\theta(x)Y} \psi_R,\end{aligned}\tag{2.8}$$

³¹⁹ where the left handed fermions form isospin doubles χ_L and the right handed fermions
³²⁰ are isosinglets ψ_R . For the first generation of leptons and quarks this represents

$$\begin{aligned}\chi_L &= \begin{pmatrix} \nu_e \\ e \end{pmatrix}_L, & \begin{pmatrix} u \\ d \end{pmatrix}_L \\ \psi_R &= e_R, & u_R, d_R\end{aligned}\tag{2.9}$$

³²¹ Imposing local gauge invariance within \mathcal{L}_{EWK} is once again achieved by modifying
³²² the covariant derivative

$$D_\mu = \partial_\mu - \frac{ig}{2} \tau^i W_\mu^i - \frac{ig'}{2} Y B_\mu,\tag{2.10}$$

³²³ where g and g' are the coupling constant of the $SU(2)_L$ and $U(1)_Y$ groups respectively.
³²⁴ Taking the example of the first generation of fermions defined in Equation.(2.9), with input
³²⁵ hypercharge values of -1 and -2 for χ_L and e_R respectively, would lead to a Lagrangian
³²⁶ \mathcal{L}_1 of the form,

$$\begin{aligned}\mathcal{L}_1 = &\bar{\chi}_L \gamma^\mu [i\partial_\mu - g \frac{1}{2} \tau \cdot W_\mu - g' (-\frac{1}{2}) B_\mu] \chi_L \\ &+ \bar{e}_R \gamma^\mu [i\partial_\mu - g' (-1) B_\mu] e_R - \frac{1}{4} W_{\mu\nu} \cdot W^{\mu\nu} - \frac{1}{4} B_{\mu\nu} B^{\mu\nu}.\end{aligned}\tag{2.11}$$

³²⁷ As in **QED**, these additional gauge fields introduce field strength tensors $B_{\mu\nu}$ and
³²⁸ $W_{\mu\nu}$,

$$\hat{B}_{\mu\nu} = \partial_\mu \hat{B}_\nu - \partial_\nu \hat{B}_\mu \quad (2.12)$$

$$\hat{W}_{\mu\nu} = \partial_\mu \hat{W}_\nu - \partial_\nu \hat{W}_\mu - g \hat{W}_\mu \times \hat{W}_\nu \quad (2.13)$$

³²⁹ corresponding to the kinetic energy and self coupling of the W_μ fields and the kinetic
³³⁰ energy term of the B_μ field.

³³¹ None of these gauge bosons are physical particles, and instead linear combinations of
³³² these gauge bosons make up γ and the W and Z bosons, defined as

$$W^\pm = \frac{1}{\sqrt{2}} (W_\mu^1 \mp i W_\mu^2) \quad \begin{pmatrix} Z_\mu \\ A_\mu \end{pmatrix} = \begin{pmatrix} \cos\theta_W & -\sin\theta_W \\ \sin\theta_W & \cos\theta_W \end{pmatrix} \begin{pmatrix} W_\mu^3 \\ B_\mu \end{pmatrix} \quad (2.14)$$

³³³ where the mixing angle, $\theta_w = \tan^{-1} \frac{g'}{g}$, relates the coupling of the neutral weak and
³³⁴ electromagnetic interactions.

³³⁵ As in the case of the formulation of the **QED** Lagrangian there remains no mass term
³³⁶ for the photon. However this is also the case for the W, Z and fermions in the Lagrangian,
³³⁷ contrary to experimental measurement. Any explicit introduction of mass terms would
³³⁸ break the symmetry of the Lagrangian and instead mass terms can be introduced through
³³⁹ spontaneous breaking of the **EWK** symmetry via the Higgs mechanism.

³⁴⁰ The Higgs mechanism induces spontaneous symmetry breaking through the introduc-
³⁴¹ tion of a complex scalar SU(2) doublet field ϕ which attains a non-zero Vacuum
³⁴² Expectation Value (**VEV**) [17][18][19][20].

$$\phi = \begin{pmatrix} \phi^+ \\ \phi^0 \end{pmatrix} \quad \text{with} \quad \begin{aligned} \phi^+ &\equiv (\phi_1 + i\phi_2)/\sqrt{2} \\ \phi^0 &\equiv (\phi_3 + i\phi_4)/\sqrt{2} \end{aligned} \quad (2.15)$$

³⁴³ The Lagrangian defined in Equation (2.11) attains an additional term \mathcal{L}_{Higgs} of the
³⁴⁴ form

$$\mathcal{L}_{Higgs} = \overbrace{(D_\mu \phi)^\dagger (D^\mu \phi)}^{\text{kinetic}} - \overbrace{\mu^2 \phi^\dagger \phi - \lambda (\phi^\dagger \phi)^2}^{\text{potential } V(\phi)} \quad (\mu^2, \lambda) > 0 \in \mathbb{R},$$

$$\mathcal{L}_{SM} = \mathcal{L}_{EWK} + \mathcal{L}_{Higgs}, \quad (2.16)$$

³⁴⁵ where the covariant derivative D_μ is that defined in Equation (2.10). The last two
³⁴⁶ terms of \mathcal{L}_{Higgs} correspond to the Higgs potential, in which positive real positive values
³⁴⁷ of μ^2 and λ are required to ensure the generation of masses for the bosons and leptons.
³⁴⁸ The minimum of this potential is found at $\phi^\dagger \phi = \frac{1}{2}(\phi_1^2 + \phi_2^2 + \phi_3^2 + \phi_4^2) = \mu^2/\lambda = v^2$,
³⁴⁹ where v represents the **VEV**.

³⁵⁰ Defining the ground state of the ϕ field to be consistent with the $V(\phi)$ minimum, and
³⁵¹ then expanding around a ground state chosen to maintain an unbroken electromagnetic
³⁵² symmetry thus preserving a zero photon mass [21] leads to

$$\phi_0 = \sqrt{\frac{1}{2}} \begin{pmatrix} 0 \\ v \end{pmatrix}, \quad \phi(x) = e^{i\tau \cdot \theta(x)/v} \sqrt{\frac{1}{2}} \begin{pmatrix} 0 \\ v + h(x) \end{pmatrix}, \quad (2.17)$$

³⁵³ where the fluctuations from the vacuum ϕ_0 are parametrized in terms of four real
³⁵⁴ fields, $\theta_1, \theta_2, \theta_3$ and $h(x)$.

³⁵⁵ Choosing to gauge away the three massless Goldstone boson fields by setting $\theta(x)$ to
³⁵⁶ zero and substituting $\phi(x)$ back into kinetic term of \mathcal{L}_{Higgs} from Equation (2.16) leads to
³⁵⁷ mass terms for the W^\pm and Z bosons

$$(D_\mu \phi)^\dagger (D^\mu \phi) = \frac{1}{2}(\partial_\mu h)^2 + \frac{g^2 v^2}{2} W_\mu^+ W^{-\mu} + \frac{v^2 g^2}{8 \cos^2 \theta_w} Z_\mu Z^\mu + 0 A_\mu A^\mu, \quad (2.18)$$

³⁵⁸ where the relations between the physical and electroweak gauge fields from Equation
³⁵⁹ (2.14) are used. The W^\pm and Z bosons can then be determined to be

$$M_W = \frac{1}{2}gv \quad M_Z = \frac{1}{2} \frac{gv}{\cos \theta_w}. \quad (2.19)$$

360 This mechanism is also used to generate fermion masses by introducing a Yukawa
 361 coupling between the fermions and the ϕ field [22], with the coupling strength of a particle
 362 to the ϕ field governing its mass. Additionally a scalar boson h with mass $m_h = v\sqrt{\frac{\lambda}{2}}$, is
 363 also predicted as a result of this spontaneous symmetry breaking and became known as
 364 the Higgs boson. Its discovery by the CMS and ATLAS experiments in 2012 is concrete
 365 evidence to support this method of mass generation within the SM.

366 2.2. Motivation for Physics Beyond the Standard 367 Model

368 As has been described, the SM has proved to be a very successful theory, predicting the
 369 existence of the W^\pm and Z bosons and the top quark long before they were experimentally
 370 observed. However the theory does not accurately describe all observed phenomena and
 371 has some fundamental theoretical flaws that hint at the need for additional extensions to
 372 the current theory.

373 On a theoretical level, the SM is unable to incorporate the gravitational interactions
 374 of fundamental particles within the theory. Whilst at the electroweak energy scales the
 375 relative strength of gravity is negligible compared to the other three fundamental forces,
 376 at much higher energy scales $M_{planck} \sim 10^{18} GeV$ quantum gravitational effects become
 377 increasingly dominant. The failure to reconcile gravity within the SM, demonstrates that
 378 the SM must become invalid at some higher energy scale.

379 Some other deficiencies with the SM include the fact that the predicted rate of
 380 Charge-Parity violation does not account for the matter dominated universe which we
 381 inhabit, and the SM prediction of zero neutrino mass conflicts with the observation of
 382 neutrino flavour mixing, attributed to mixing between neutrino mass eigenstates [23][24].

383 Perhaps one of the most glaring gaps in the predictive power of the SM is that there
 384 exists no candidate to explain the cosmic dark matter observed in galactic structures
 385 through indirect techniques including gravitational lensing and measurement of the
 386 orbital velocity of stars in galactic edges. Any such candidate must be very weakly

387 interacting which must also be stable, owing to the lack of direct detection of the decay
388 products of such an process. Providing a dark matter candidate is of the prime goals
389 which be tackled by any Beyond Standard Model (**BSM**) physics model.

390 The recent discovery of the Higgs boson whilst a significant victory for the predictive
391 power of the **SM**, brings with it still unresolved questions. This issue is commonly
392 described as the “hierarchy problem”.

393 In the absence of new physics between the TeV and Planck scale, calculating beyond
394 tree-level contributions to the Higgs mass term given by its self interaction, result in
395 divergent terms that push the Higgs mass up to the planck mass M_{planck} .

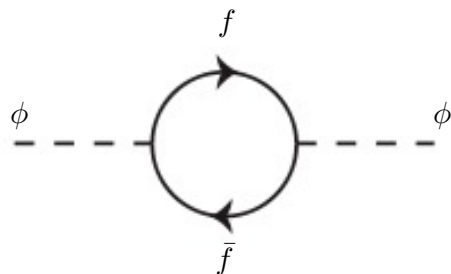


Figure 2.1.: One loop quantum corrections to the Higgs squared mass parameter m_h^2 due to a fermion.

396 This can be demonstrated by considering the one loop quantum correction to the
397 Higgs mass with a fermion f , shown in Figure 2.1 with mass m_f . The Higgs field couples
398 to f with a term in the Lagrangian $-\lambda_f h \bar{f} f$, yielding a correction of the form [25],

$$\delta m_h^2 = -\frac{|\lambda_f|^2}{8\pi^2} \Lambda^2 + \dots, \quad (2.20)$$

399 where λ_f represents the coupling strength for each type of fermion $\propto m_f$, and Λ the
400 cutoff energy scale at which the **SM** ceases to be a valid theory.

401 To recover the mass of the now discovered Higgs boson would require a fine-tuning of
402 the parameters to cancel out these mass corrections the the Higgs mass to the scale of
403 30 orders of magnitude. This appears as an unnatural solution to physicists and it is
404 this hierarchy problem that provides one of the strongest motivations for the theory of
405 SUperSYmmetry (**SUSY**).

⁴⁰⁶ 2.3. Supersymmetry Overview

⁴⁰⁷ Supersymmetry provides potential solutions to many of the issues raised in the previous
⁴⁰⁸ section. It provides a dark matter candidate, can explain baryogenesis in the early
⁴⁰⁹ universe and also provides an elegant solution to the hierarchy problem [26][27][28][29].
⁴¹⁰ At its heart it represents a new space-time symmetry that relates fermions and bosons.
⁴¹¹ This symmetry converts bosonic states into fermionic states, and vice versa, see Equation
⁴¹² (2.21) ,

$$Q|Boson\rangle = |Fermion\rangle \quad Q|Fermion\rangle = |Boson\rangle, \quad (2.21)$$

⁴¹³ where the operator Q is the generator of these transformations. Quantum field theories
⁴¹⁴ which are invariant under such transformations are called supersymmetric.

⁴¹⁵ This symmetry operator therefore acts upon a particles spin altering it by a half integer
⁴¹⁶ value. The consequences of the introduction of this additional space-time symmetry
⁴¹⁷ introduce a new rich phenomenology. For example in supersymmetric theories, both
⁴¹⁸ the left handed $SU(2)$ doublet and right handed singlet of fermions will have a spin-0
⁴¹⁹ superpartner, containing the same electric charge, weak isospin, and colour as its **SM**
⁴²⁰ partner. In the case of the leptons $(\nu_l, l)_L$ will have two superpartners, a sneutrino $\tilde{\nu}_l{}_L$
⁴²¹ and a slepton \tilde{l}_L , whilst the singlet l_R also has a superpartner slepton \tilde{l}_R .

⁴²² Each particle in a supersymmetric theory is paired together with their superpartners
⁴²³ as a result of this supersymmetric transformations in a so called supermultiplet. These
⁴²⁴ superpartners will then consequently also contribute to the corrections to the Higgs mass.
⁴²⁵ Bosonic and fermionic loops contributing to the correction appear with opposite signs,
⁴²⁶ and therefore cancellation of these divergent terms will stabilise the Higgs mass, solving
⁴²⁷ the hierarchy problem [30][31].

⁴²⁸ One of the simplest forms of **SUSY** would predict a whole set of supersymmetric
⁴²⁹ partners to their **SM** counterparts with the same mass and interactions. However the
⁴³⁰ currently lack of any experimental evidence for the predicted sparticle spectrum implies
⁴³¹ **SUSY** must be a broken symmetry in which any sparticle masses must be greater than
⁴³² their SM counterparts.

⁴³³ There exist many techniques which can induce supersymmetric breaking [32][33][34].
⁴³⁴ Of particular interest to experimental physicists are those at which the breaking scale

⁴³⁵ is of an order that is experimentally accessible to the LHC i.e. \sim TeV scale. Whilst
⁴³⁶ there is no requirement for supersymmetric breaking to occur at this energy scale, for
⁴³⁷ supersymmetry to provide a solution to the hierarchy problem, it is necessary for this
⁴³⁸ scale to not differ too drastically from the EWK scale [35][36].

⁴³⁹ 2.3.1. R-Parity

⁴⁴⁰ Some supersymmetric theories also present a solution to the dark matter problem. Such
⁴⁴¹ theories can contain a Lightest Supersymmetric Partner (LSP), which matches the criteria
⁴⁴² of a Weakly Interacting Massive Particle (WIMP) required by cosmological observation
⁴⁴³ if R-parity is conserved.

⁴⁴⁴ Baryon (B) and Lepton (L) number conservation is forbidden in the SM by renor-
⁴⁴⁵ malisability requirements. The violation of Baryon or Lepton number would result in
⁴⁴⁶ the proton lifetime much shorter than those set by experimental limits [37]. Another
⁴⁴⁷ symmetry called R-parity is then often introduced to SUSY theories to maintain baryon
⁴⁴⁸ and lepton conservation.

⁴⁴⁹ R-parity is described by the equation

$$R_P = (-1)^{3(B-L)+2s}, \quad (2.22)$$

⁴⁵⁰ where s represents the spin of the particles. $B = \pm \frac{1}{3}$ for quarks/antiquarks and $B = 0$
⁴⁵¹ for all others, $L = \pm 1$ for leptons/antileptons, $L = 0$ for all others.

⁴⁵² R-parity ensures the stability of the proton in SUSY models, and also has other
⁴⁵³ consequences for the production and decay of supersymmetric particles. At particle
⁴⁵⁴ colliders supersymmetric particles can only be pair produced, and similarly the decay
⁴⁵⁵ of any produced supersymmetric particle is restricted to a SM particle and a lighter
⁴⁵⁶ supersymmetric particle as allowed by conservation laws. A further implication of R-
⁴⁵⁷ parity is that once a supersymmetric particle has decayed to the LSP it remains stable,
⁴⁵⁸ unable to decay into a SM particle.

⁴⁵⁹ A LSP would not interact in a detector at a particle collider, leaving behind a missing
⁴⁶⁰ energy \cancel{E}_T signature. The assumption of R-parity and its consequences are used to
⁴⁶¹ determine the physical motivation and search strategies for SUSY model at the LHC.

462 2.4. Experimental signatures of SUSY at the LHC

463 Should strongly interacting sparticles be within the experimental reach of the LHC, then
464 it is expected that they can be produced in a variety of ways.

- 465 • squark/anti-squark and gluino pairs can be produced via both gluon fusion and
466 quark/anti-quark scattering.
- 467 • a gluino and squark produced together via quark-gluon scattering
- 468 • squark pairs produced via quark-quark scattering

469 Whilst most SUSY searches invoke the requirement of R-parity to explore parameter
470 phase space, there still exist a whole plethora of possible SUSY model topologies which
471 could be discovered at the LHC.

472 During the 2011 run period at a $\sqrt{s} = 7$ TeV particular models were used to benchmark
473 performance and experimental reach of both CMS searches and previous experiments.
474 The Compressed Minimal SuperSymmetric Model (CMSSM) was initially chosen for a
475 number of reasons [38]. One of the most compelling being the reduction from the up to
476 105 new parameters introduced by SUSY in addition to the existing 19 of the SM to that
477 of just 5 free extra free parameters. It was this simplicity, combined with the theory not
478 requiring any fine tuning of particle masses to produce the experimentally verified SM
479 that made it an attractive model to interpret physics results.

480 However recent results from the LHC now strongly disfavour large swathes of CMSSM
481 parameter space [39][40][41]. In the face of such results a more pragmatic model indepen-
482 dent search strategy is now applied across most SUSY searches at the LHC, see Section
483 (2.4.1).

484 As previously stated, a stable LSP that exhibits the properties of a dark matter would
485 be weakly interacting and therefore will not be directly detected in a detector environment.
486 Additionally the cascade decays of supersymmetric particles to the LSP would also result
487 in significant hadronic activity. These signatures can then be characterised through
488 large amounts of hadronic jets (see Section (3.3.1)), leptons and a significant amount of
489 missing energy dependent upon the size of the mass splitting between the LSP and the
490 supersymmetric particle it has decayed from.

491 Whilst the SM contains processes which can exhibit a similar event topology to that
492 described above. The largest contribution of which comes in from the general QCD

493 environment of a hadron collider. A multitude of different analytical techniques are used
494 by experimental physicists to reduce or estimate any reducible or irreducible backgrounds,
495 allowing a possible **SUSY** signature to be extracted. The techniques employed within
496 this thesis are described in great detail within Section (4.1).

497 2.4.1. Simplified Models

498 With such a variety of different ways for a **SUSY** signal to manifest itself, it is necessary
499 to be able to interpret experimental reach through the masses of gluinos and squarks
500 which can excluded by experimental searches rather than on a model specific basis.

501 This is accomplished through **SMS** models, which are defined by a set of hypothetical
502 particles and a sequence of their production and decay [42][43]. In the **SMS** models
503 considered within this thesis, only the production process for the two primary particles
504 are considered. Each primary particle can undergo a direct or a cascade decay through
505 an intermediate new particle. At the end of each decay chain there remains a neutral,
506 undetected **LSP** particle, denoted $\tilde{\chi}_{LSP}$ which can represent a neutralino or gravitino.
507 Essentially it is easier to consider each **SMS** with branching ratios set to 100% The
508 masses of the primary particle and the **LSP** remain as free parameters, in which the
509 absolute value and relative difference between the primary and **LSP** particle alter the
510 kinematics of the event.

511 Different **SMS** models are denoted with a T-prefix, with a summary of the types
512 interpreted within this thesis listed below [44].

- 513 • **T1,T1xxxx**, models represent a simplified version of gluino pair production with
514 each gluino (superpartner to the gluon) undergoing a three-body decay to a quark-
515 antiquark pair and the **LSP** (i.e. $\tilde{g} \rightarrow q\bar{q}\tilde{\chi}_{LSP}$). The resultant final state from this
516 decay is typically 4 jets + \cancel{E}_T in the absence of initial/final state radiation and
517 detector effects. xxxx denotes models in which the quarks are of a specific flavour,
518 typically t or b quark-antiquarks.
- 519 • **T2,T2xx**, models represent a simplified version of squark anti-squark production
520 with each squark undergoing a two-body decay into a light-flavour quark and **LSP**
521 (i.e. $\tilde{q} \rightarrow q\tilde{\chi}_{LSP}$). This results in final states with less jets than gluino mediated
522 production, typically 2 jets + \cancel{E}_T when again ignoring the effect of initial/final state
523 radiation and detector effects. xx models again represent decays in which both the
524 quark and the squark within the decay is of a specific flavour, typically \tilde{t}/t or \tilde{b}/b .

Models rich in b and t quarks are interpreted within this thesis as they remain of particular interest within “Natural SUSY” scenarios [45][46]. The largest contribution to the quadratic divergence in the Higgs mass parameter comes from a loop of top quarks via the Yukawa coupling. Cancellation of these divergences can be achieved in supersymmetric theories by requiring a light right handed top squark, \tilde{t}_R , and left-handed double $SU(2)_L$ doublet containing top and bottom squarks, $(\tilde{\frac{t}{b}})_L$ [47].

These theories therefore solve the hierarchy problem by predicting light \sim EWK scale third generation sleptons, to be accessible at the LHC. Search strategies involving the requirement of b-tagging (see Section (3.3.2)) are used to give sensitivity to these type of SUSY scenarios and are discussed in greater detail within Chapter 5.

Two example decay chains are shown in Figure 2.2; the pair production of gluinos (T1) and the pair production of squarks (T2) decaying into SM particles and LSP’s.

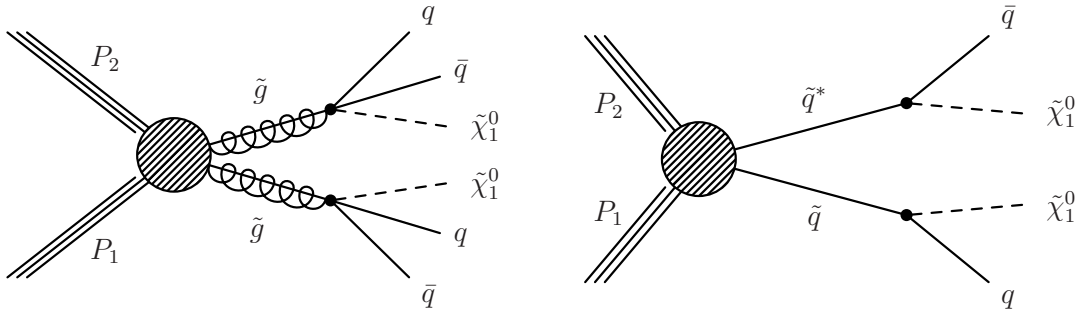


Figure 2.2.: Two example SMS model decays (T1 (left), T2 (right)), which are used in interpretations of physics reach by CMS.

Chapter 3.

⁵³⁷ The LHC and the CMS Detector

⁵³⁸ Probing the SM for signs of new physics would not be possible without the immensely
⁵³⁹ complex electronics and machinery that makes the TeV energy scale accessible for the
⁵⁴⁰ first time. This chapter will cover the LHC based at European Organization for Nuclear
⁵⁴¹ Research (CERN) and the Compact Muon Solenoid (CMS) detector, being the experiment
⁵⁴² the author is a member of. Section (3.2) serves to introduce an overview of the different
⁵⁴³ components of the CMS detector, with more detail spent on those that are relevant in
⁵⁴⁴ the search for Supersymmetric particles. Section (3.3) will focus on event and object
⁵⁴⁵ reconstruction again with more emphasis on jet level quantities which are most relevant
⁵⁴⁶ to the author's analysis research. Finally Section (3.4) will cover work performed by
⁵⁴⁷ the author, as service to the CMS Collaboration, in measuring the performance of the
⁵⁴⁸ Global Calorimeter Trigger (GCT) component of the L1 trigger during the 2012-2013
⁵⁴⁹ run period.

⁵⁵⁰ 3.1. The LHC

⁵⁵¹ The LHC is a storage ring, accelerator, and collider of circulating beams of protons or
⁵⁵² ions. Housed in the tunnel dug for the Large Electron-Positron collider (LEP), it is
⁵⁵³ approximately 27 km in circumference, 100 m underground, and straddles the border
⁵⁵⁴ between France and Switzerland outside of Geneva. It is currently the only collider
⁵⁵⁵ in operation that is able to study physics at the TeV scale. A double-ring circular
⁵⁵⁶ synchrotron, it was designed to collide both proton-proton (pp) and heavy ion (PbPb)
⁵⁵⁷ with a centre of mass energy $\sqrt{s} = 14$ TeV at a final design luminosity of $10^{34}\text{cm}^{-2}\text{s}^{-1}$.

⁵⁵⁸

These counter-circulating beams of protons/Pb ions are merged in four sections around the ring to enable collisions of the beams, with each interaction point being home to one of the four major experiments; A Large Ion Collider Experiment (**ALICE**) [48], A Toroidal LHC ApparatuS (**ATLAS**) [49], Compact Muon Solenoid (**CMS**) [50] and Large Hadron Collider Beauty (**LHC-B**) [51] which record the resultant collisions. The layout of the **LHC** ring is shown in Figure 3.1. The remaining four sections contain acceleration, collimation and beam dump systems. In the eight arc sections, the beams are steered by magnetic fields of up to 8 T provided by super conduction dipole magnets, which are maintained at temperatures of 2 K using superfluid helium. Additional magnets for focusing and corrections are also present in straight sections within the arcs and near the interaction regions where the detectors are situated.

570

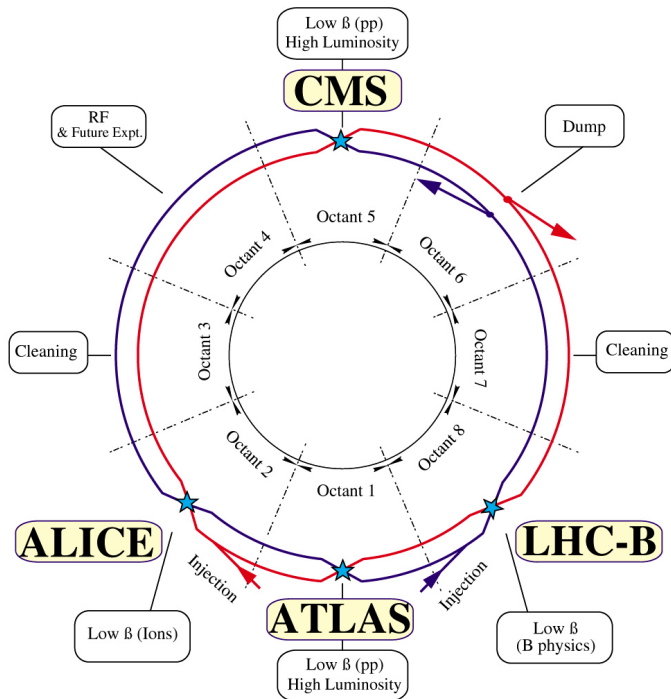


Figure 3.1.: A top down layout of the LHC. [52], with the position of the four main detectors labelled.

Proton beams are formed inside the Proton Synchrotron (**PS**) from bunches of protons 50 ns apart with an energy of 26 GeV. The protons are then accelerated in the Super Proton Synchrotron (**SPS**) to 450 GeV before being injected into the **LHC**. These **LHC** proton beams consists of many “bunches” i.e. approximately 1.1×10^{11} protons localized into less than 1 ns in the direction of motion. Before collision the beams are ramped to 4

576 TeV (2012) per beam in a process involving increasing the current passing through the
 577 dipole magnets. Once the desired \sqrt{s} energy is reached then the beams are allowed to
 578 collide at the interaction points. The luminosity falls regularly as the run progresses as
 579 protons are lost in collisions, and eventually the beam is dumped before repeating the
 580 process again.

581

582 Colliding the beams produced an instantaneous luminosity of approximately $5 \times$
 583 $10^{33} \text{ cm}^{-2}\text{s}^{-1}$ during the 2012 run. The high number of protons in each bunch increases
 584 the likelihood of multiple interactions with each crossing of the counter-circulating
 585 beams. This leads to isotropic energy depositions within the detectors positioned at these
 586 interaction points, increasing the energy scale of the underlying event. This is known as
 587 pile-up and the counteracting of it's effects are important to the many measurements
 588 performed at the LHC.

589 In the early phase of prolonged operation after the initial shutdown the machine
 590 operated in 2010-2011 at 3.5 TeV per beam, $\sqrt{s} = 7 \text{ TeV}$, delivering 6.13 fb^{-1} of data
 591 [53]. During the 2012-2013 run period, data was collected at an increased $\sqrt{s} = 8 \text{ TeV}$
 592 improving the sensitivity of searches for new physics. Over the whole run period 23.3
 593 fb^{-1} of data was delivered of which 21.8 fb^{-1} was recorded by the CMS detector as shown
 594 in Figure 3.2 [53]. A total of 12 fb^{-1} of 8 TeV certified data was collected by October
 595 2012, and it is this data which forms the basis of the results discussed within this thesis.

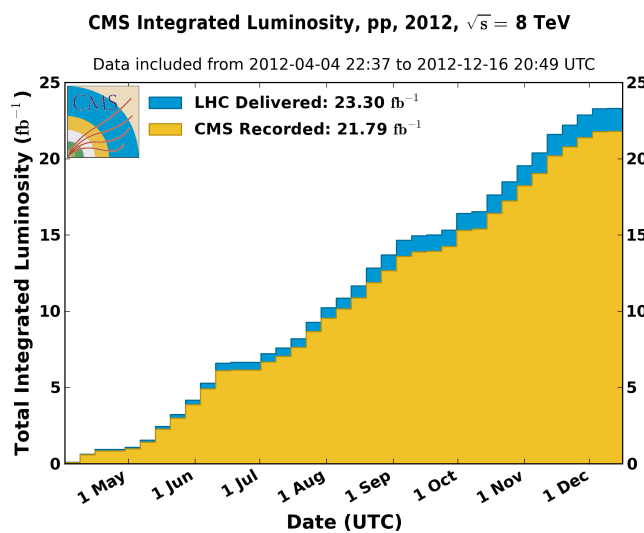


Figure 3.2.: The total integrated luminosity delivered to and collected by CMS during the 2012 8 TeV pp runs.

⁵⁹⁶ 3.2. The CMS detector

⁵⁹⁷ The Compact Muon Solenoid (**CMS**) detector is one of two general purpose detectors
⁵⁹⁸ at the **LHC** designed to search for new physics. The detector is designed to provide
⁵⁹⁹ efficient identification and measurement of many physics objects including photons,
⁶⁰⁰ electrons, muons, taus, and hadronic showers over wide ranges of transverse momentum
⁶⁰¹ and direction. Its nearly 4π coverage in solid angle allows for accurate measurement of
⁶⁰² global transverse momentum imbalance. These design factors give **CMS** the ability to
⁶⁰³ search for direct production of **SUSY** particles at the TeV scale, making the search for
⁶⁰⁴ Supersymmetric particles one of the highest priorities among the wide range of physics
⁶⁰⁵ programmes at **CMS**.

⁶⁰⁶

⁶⁰⁷ **CMS** uses a right-handed Cartesian coordinate system with the origin at the interaction
⁶⁰⁸ point and the z-axis pointing along the beam axis, the x-axis points radially inwards to
⁶⁰⁹ the centre of the collider ring, with the y-axis points vertically upward. The azimuthal
⁶¹⁰ angle, ϕ ranging between $[-\pi, \pi]$ is defined in the x-y plane starting from the x-axis. The
⁶¹¹ polar angle θ is measured from the z axis. The common convention in particle physics is
⁶¹² to express an out going particle in terms of ϕ and its pseudorapidity defined as

$$\eta = -\log \tan \left(\frac{\theta}{2} \right). \quad (3.1)$$

⁶¹³ The variable $\Delta R = \sqrt{\Delta\phi^2 + \Delta\eta^2}$ is commonly used to define angular distance
⁶¹⁴ between objects within the detector and additionally energy and momentum is typically
⁶¹⁵ measured in the transverse plane perpendicular to the beam line. These values are
⁶¹⁶ calculated from the x and y components of the object and are denoted as $E_T = E \sin \theta$
⁶¹⁷ and $p_T = \sqrt{p_x^2 + p_y^2}$.

⁶¹⁸ 3.2.1. Detector Subsystems

⁶¹⁹ As the range of particles produced in pp collisions interact in different ways with mat-
⁶²⁰ ter, **CMS** is divided into subdetector systems, which perform complementary roles to
⁶²¹ identify the identity, mass and momentum of the different physics objects present in
⁶²² each event. These detector sub-systems contained inside **CMS** are wrapped in layers

623 around a central 13 m long 4 T super conducting solenoid as shown in Figure 3.3. With
 624 the endcaps closed , CMS is a cylinder of length 22 m, diameter 15 m, and mass 12.5
 625 kilotons. A more detailed complete description of the detector can be found elsewhere [50].

626

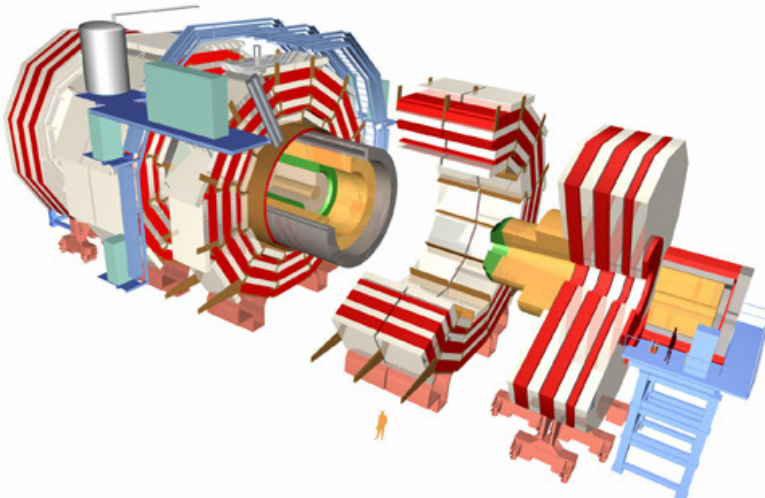


Figure 3.3.: A pictorial depiction of the CMS detector with the main detector subsystems labelled. [54]

627 3.2.2. Tracker

628 The inner-most subdetector of the barrel is the multi-layer silicon tracker, formed of a
 629 pixel detector component encased by layers of silicon strip detectors. The pixel detector
 630 consists of three layers of silicon pixel sensors providing measurements of the momentum,
 631 position coordinates of the charged particles as they pass, and the location of primary
 632 and secondary vertices between 4cm and 10cm transverse to the beam. Outside the pixel
 633 detector, ten cylindrical layers of silicon strip detectors extend the tracking system out to
 634 a radius of 1.20m from the beam line. The tracking system provides efficient and precise
 635 determination of the charges, momenta, and impact parameters of charged particles with
 636 the geometry of the tracker extending to cover a rapidity range up to $|\eta| < 2.5$.

637

638 The tracking system also plays a crucial part in the identification of jets originating
 639 from b-quarks through measurement of displaced secondary vertices, which is covered in
 640 more detail in Section (3.3.2). The identification of b-jets is important in many searches

641 for natural SUSY models and forms an important part of the inclusive search strategy
642 described within Section (4.2).

643 **3.2.3. Electromagnetic Calorimeter**

644 Immediately outside of the tracker, but still within the magnet core, sits the Electromag-
645 netic CALorimeter (**ECAL**). Covering a pseudorapidity up to $|\eta| < 3$ and comprising
646 of over 75,000 PbWO₄ (lead tungstate) crystals that scintillate as particles deposit energy,
647 the **ECAL** provides high resolution measurements of the electromagnetic showers from
648 photons, electrons in the detector.

649

650 Lead tungstate is used because of its short radiation length ($X_0 \sim 0.9\text{cm}$) and small
651 Molieré radius ($\sim 2.1\text{cm}$) leading to high granularity and resolution. It's fast scintillation
652 time ($\sim 25\text{ns}$) reduces the effects of pile-up due to energy from previous collisions still
653 being read out, and its radiation hardness gives it longevity. The crystals are arranged
654 in modules which surround the beam line in a non-projective geometry, angled at 3°
655 with respect to the interaction point to minimise the risk of particles escaping down the
656 cracks between the crystals.

657

658 The **ECAL** is primarily composed of two sections, the Electromagnetic CALorime-
659 ter Barrel (**EB**) which extends in pseudo-rapidity to $|\eta| < 1.479$ with a crystal front
660 cross section of $22 \times 22\text{ mm}^2$ and a length of 230 mm corresponding to 25.8 radia-
661 tion lengths, and the Electromagnetic CALorimeter Endcap (**EE**) covering a rapidity
662 range of $1.479 < |\eta| < 3.0$, which consists of two identical detectors on either side of
663 the **EB**. A lead-silicon sampling ‘pre-shower’ detector Electromagnetic CALorimeter
664 pre-Shower (**ES**) is placed before the endcaps to aid in the identification of neutral pions.
665 Their arrangement are shown in Figure 3.4.

666

667 Scintillation photons from the lead tungstate crystals are instrumented with Avalanche
668 Photo-Diodes (**APD**) and Vacuum Photo-Triodes (**VPT**) located in the **EB** and **EE**
669 respectively, converting the scintillating light into an electric signal which is consequently
670 used to determine the amount of energy deposited within the crystal . These instruments
671 are chosen for their resistance under operation to the strong magnetic field of **CMS**. The
672 scintillation of the **ECAL** crystals as well as the response of the **APDs** varies as a function

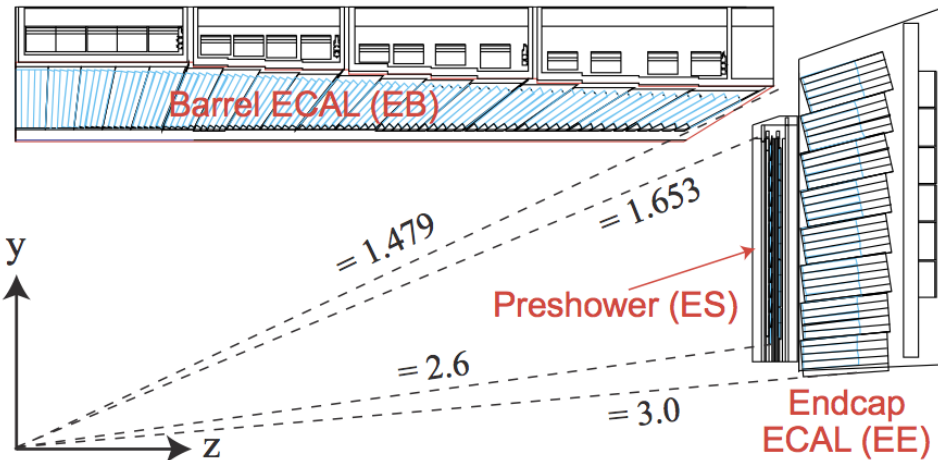


Figure 3.4.: Illustration of the CMS ECAL showing the arrangement of the lead tungstate crystals in the EB and EE. The ES is also shown and is located in front of the EE [55].

673 of temperature and so cooling systems continually maintain an overall constant ECAL
 674 temperature $\pm 0.05^\circ C$.

675 3.2.4. Hadronic Calorimeter

676 Beyond the ECAL lies the Hadronic CALorimeter (HCAL) which is responsible for
 677 the accurate measurement of hadronic showers, crucial for analyses involving jets or
 678 missing energy signatures. The HCAL is a sampling calorimeter which consists of al-
 679 ternating layers of brass absorber and plastic scintillator, except in the hadron forward
 680 ($3.0 < |\eta| < 5.0$) region in which steel absorbers and quartz fibre scintillators are used
 681 because of their increased radiation tolerance. Hadron showers are initiated in the
 682 absorber layers inducing scintillation in the plastic scintillator tiles. These scintillation
 683 photons are converted by wavelength shifting fibres for read-out by hybrid photodiodes.
 684

685 The HCAL's size is constrained to a compact size by the presence of the solenoid,
 686 requiring the placement of an additional outer calorimeter on the outside of the solenoid
 687 to increase the sampling depth of the HCAL. A schematic of the HCAL can be seen in
 688 Figure 3.5.
 689

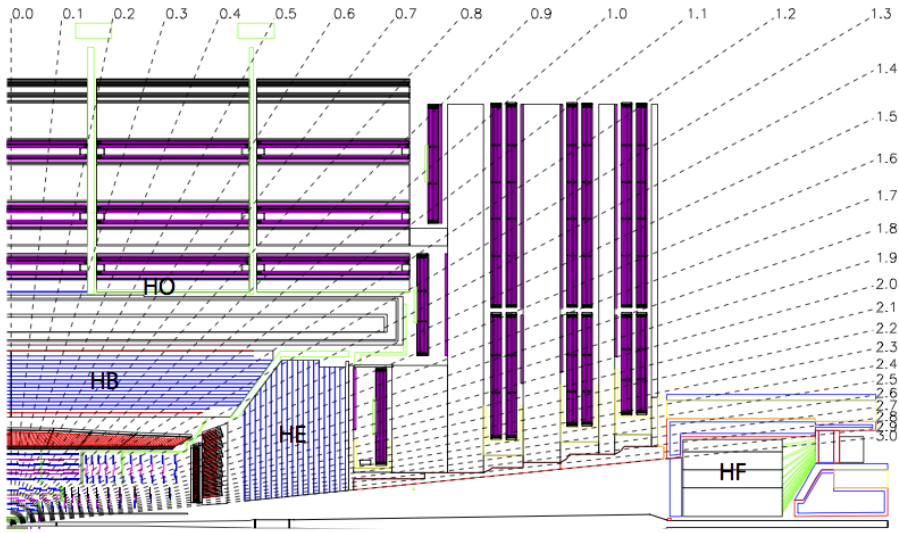


Figure 3.5.: Schematic of the hadron calorimeters in the r - z plane, showing the locations of the **HCAL** components and the **HF**. [50].

690 The **HCAL** covers the range $|\eta| < 5$ and consists of four subdetectors: the Hadron
 691 Barrel (**HB**) $|\eta| < 1.3$, the Hadron Outer (**HO**), the Hadron Endcaps (**HE**) $1.3 < |\eta| < 3.0$
 692 and the Hadron Forward (**HF**). The **HB** is contained between the outer edge of the
 693 **ECAL** and the inner edge of the solenoid, formed of 36 azimuthal wedges it is split
 694 between two half-barrel segments. The relatively short number of interaction lengths (λ_l ,
 695 the distance a hadron will travel through the absorber material before it has lost $\frac{1}{e}$ of
 696 its energy) within the **HB**, the lowest being $\lambda_l = 5.82$ for $|\eta| = 0$, facilitates the need
 697 for the ‘tail catching’ **HO** to increase the sampling depth in the central barrel rapidity
 698 region $|\eta| < 1.3$ to 11 interaction lengths . Significant fractions of the hadrons energy will
 699 be deposited in the **ECAL** as it passed through the detector. Therefore measurements
 700 of hadron energies in the central regions $|\eta| < 3.0$ use both the **ECAL** and **HCAL** to
 701 reconstruct the true energy from showering hadrons.

702 3.2.5. Muon Systems

703 Muons being too massive to radiate away energy via Bremsstrahlung, interact little in
 704 the calorimeters and mostly pass through the detector until they reach the system of
 705 muon detectors which forms the outer most part of the **CMS** detector.

706 Outside of the superconducting solenoid are four muon detection layers interleaved
707 with the iron return yokes which measure the muons energy via ionisation of gas within
708 detector elements. Three types of gaseous chamber are used. The Drift Tube (**DT**),
709 Cathode Stripe Chamber (**CSC**), and Resistive Plate Chamber (**RPC**) systems provide
710 efficient detection of muons with pseudo-rapidity $|\eta| < 2.4$. The best reconstruction
711 performance is obtained when the muon chamber is combined with the inner tracking
712 information to determine muon trajectories and their momenta [56].

713

714 **3.3. Event Reconstruction and Object Definition**

715 The goal of event reconstruction is to take the raw information recorded by the detector
716 and to compute from it higher-level quantities which can be used at an analysis level.
717 These typically correspond to an individual particle’s energy and momenta, or groups of
718 particles which shower in a narrow cone and the overall global energy and momentum
719 balance of the event. The reconstruction of these objects are described in great detail in
720 [57], however covered below are brief descriptions of those which are most relevant to the
721 analysis detailed in Section (4).

722 **3.3.1. Jets**

723 Quarks and gluons are produced copiously at the LHC in the hard scattering of partons.
724 As these quarks and gluons fragment, they hadronise and decay into a group of strongly
725 interactive particles and their decay products. These streams of particles travel in the
726 same direction, as they have been “boosted” by the momentum of the primary hadron.
727 These collections of decay products are reconstructed and identified together as a “jet”.

728 At **CMS** jets are reconstructed from energy deposits in the detector using the anti-kt
729 algorithm [58] with size parameter $\Delta R = 0.5$. The anti-kt jet algorithm clusters jets by
730 defining a distance between hard (high p_T) and soft (low p_T) particles such that soft
731 particles are preferentially clustered with hard particles before being clustered between
732 themselves. This produces jets which are robust to soft particle radiation from the pile-up
733 conditions experienced at the **LHC**.

734

735 There are two main type of jet reconstruction used at **CMS**, Calorimeter (Calo) and
736 Particle Flow (PF) jets [59]. Calorimeter jets are reconstructed using both the **ECAL**
737 and **HCAL** cells, combined into calorimeter towers . These calorimeter towers consist of
738 geometrically matched **HCAL** cells and **ECAL** crystals. Electronics noise is suppressed by
739 applying a threshold to the calorimeter cells, with pile-up effects reduced by a requirement
740 placed on the tower energy [60]. Calorimter jets are the jets used within the analyses
741 described in this thesis.

742 PF jets are formed from combining information from all of the **CMS** subdetectors
743 systems to determine which final state particles are present in the event. Generally,
744 any particle is expected to produce some combination of a track in the silicon tracker,
745 a deposit in the calorimeters, or a track in the muon system. The PF jet momentum
746 and spatial resolutions are greatly improved with respect to calorimeter jets, as the use
747 of the tracking detectors and of the high granularity of **ECAL** allows resolution and
748 measurement of charged hadrons and photons inside a jet, which together constitute \sim
749 85% of the jet energy [61].

750 The jets reconstructed by the clustering algorithm in **CMS** typically have an energy
751 that differs to the ‘true’ energy measured by a perfect detector. This stems from the
752 non-linear and nonuniform response of the calorimeters as well as other residual effects
753 including pile-up and underlying events, and therefore additional corrections are applied
754 to recover a uniform relative response as a function of pseudo-rapidity. These are applied
755 as separate sub corrections [62].

- 756 • A PU correction is first applied to the jet. It subtracts the average extra energy
757 deposited in the jet that comes from other vertices present in the event and is
758 therefore not part of the hard jet itself.
- 759 • p_T and η dependant corrections derived from Monte Carlo simulations are used to
760 account for the non-uniform response of the detector.
- 761 • p_T and η residual corrections are applied to data only to correct for difference
762 between data and Monte Carlo. The residual is derived from QCD dijet samples
763 and the p_T residual from $\gamma+$ jet and $Z+$ jets samples in data.

⁷⁶⁴ **3.3.2. B-tagging**

⁷⁶⁵ The decays of b quarks are suppressed by small CKM matrix elements. As a result, the
⁷⁶⁶ lifetimes of b-flavoured hadrons, produced in the fragmentation of b quarks, are relatively
⁷⁶⁷ long; \mathcal{O} 1ps. The identification of jets origination from b quarks is very important for
⁷⁶⁸ searches for new physics and for measurements of standard model processes.

⁷⁶⁹

⁷⁷⁰ Many different algorithms developed by CMS select b-quark jets based on variables
⁷⁷¹ such as the impact parameters of the charged-particle tracks, the properties of recon-
⁷⁷² structed decay vertices, and the presence or absence of a lepton, or combinations thereof
⁷⁷³ [63]. One of the most efficient of which is the Combined Secondary Vertex (CSV) which
⁷⁷⁴ operates based on secondary vertex and track-based lifetime information, benchmarked
⁷⁷⁵ in ‘Loose’, ‘Medium’ and ‘Tight’ working points, of which the medium point is the tagger
⁷⁷⁶ used within the α_T search detailed in Section (4.1).

⁷⁷⁷ Using the CSV tagger, a likelihood-based discriminator distinguishes between jets
⁷⁷⁸ from b-quarks, and those from charm or light quarks and gluons, which is shown in Figure
⁷⁷⁹ 3.6. The minimum thresholds on the discriminator for each working point correspond to
⁷⁸⁰ the misidentification probability for light-parton jets of 10%, 1%, and 0.1%, respectively,
⁷⁸¹ in jets with an average p_T of about 80 GeV.

⁷⁸² The b-tagging performance is evaluated to measure the b-jet tagging efficiency ϵ_b ,
⁷⁸³ and the misidentification probability of charm ϵ_c and light-parton jets ϵ_s . The tagging
⁷⁸⁴ efficiencies for each of these three jet flavours are compared between data and MC
⁷⁸⁵ simulation, from which a series of p_T and $|\eta|$ binned jet corrections are determined,

$$SF_{b,c,s} = \frac{\epsilon_{b,c,s}^{data}}{\epsilon_{b,c,s}^{MC}}. \quad (3.2)$$

⁷⁸⁶ These are collectively named ‘Btag Scale Factors’ and allow MC simulation to accu-
⁷⁸⁷ rately reflect the running conditions and performance of the tagging algorithm in data.
⁷⁸⁸ Understanding of the b-tagging efficiency is essential in order to minimise systematic
⁷⁸⁹ uncertainties in physics analyses that employ b-tagging.

⁷⁹⁰

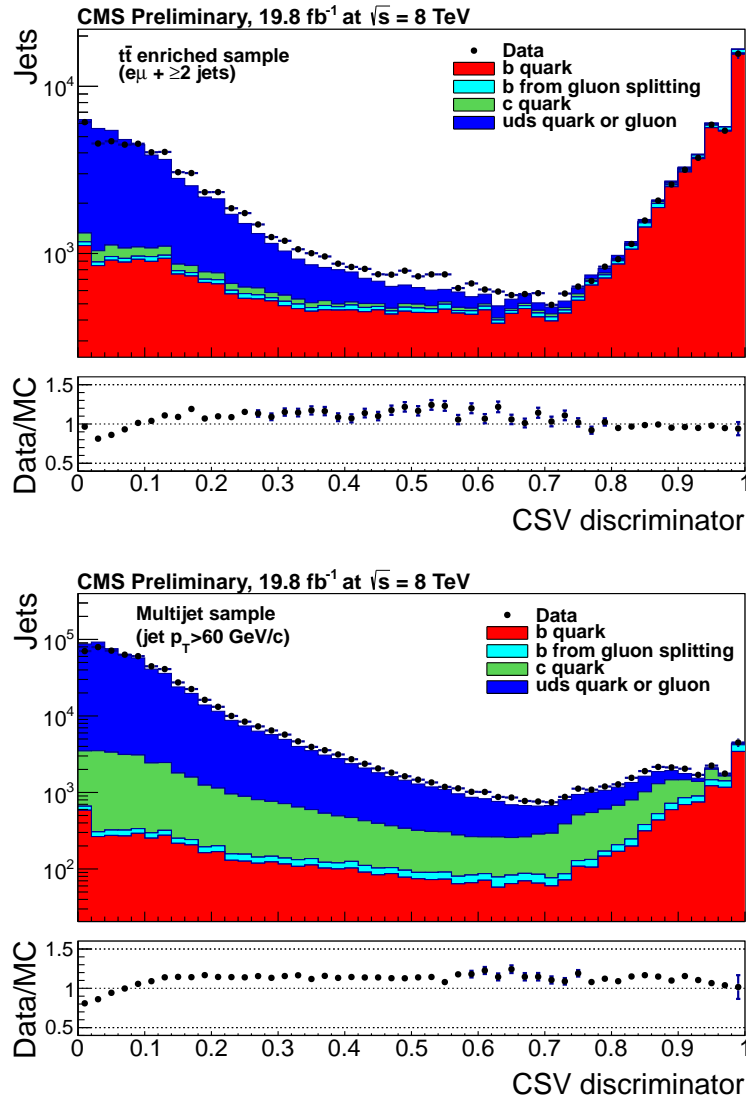


Figure 3.6.: CSV algorithm discriminator values in enriched $t\bar{t}$ bar (top) and inclusive multi jet samples (bottom) for b,c and light flavoured jets [64]. Working points are determined from the misidentification probability for light-parton jets to be tagged as a b-jet and are given as 0.244, 0.679 and 0.898 for L,M and T working points respectively.

791 The b-tagging efficiency is measured in data using several methods applied to multi
 792 jet events, primarily based on a sample of jets enriched in heavy flavour content. One
 793 method requires the collection of events with a soft muon within a cone $\Delta R < 0.4$ around
 794 the jet axis. Because the semileptonic branching fraction of b hadrons is significantly
 795 larger than that for other hadrons, these jets are more likely to arise from b quarks than
 796 from another flavour, with the resultant momentum component of the muon transverse
 797 to the jet axis larger for muons from b-hadron decays than from light or charm jets.

Additionally the performance of the tagger can also be benchmarked in $t\bar{t}$ events where in the SM, the top quark is expected to decay to a W boson and a b quark about 99.8% of the time [1]. Further selection criteria is applied to these events to further enrich the b quark content of these events. The methods to identify b-jets in data are discussed in great detail at [65]. The jet flavours are determined in simulation using truth level information and are compared to data to determine the correction scale factors (SF_b), which are displayed for the CSVM tagger in Figure 3.7.

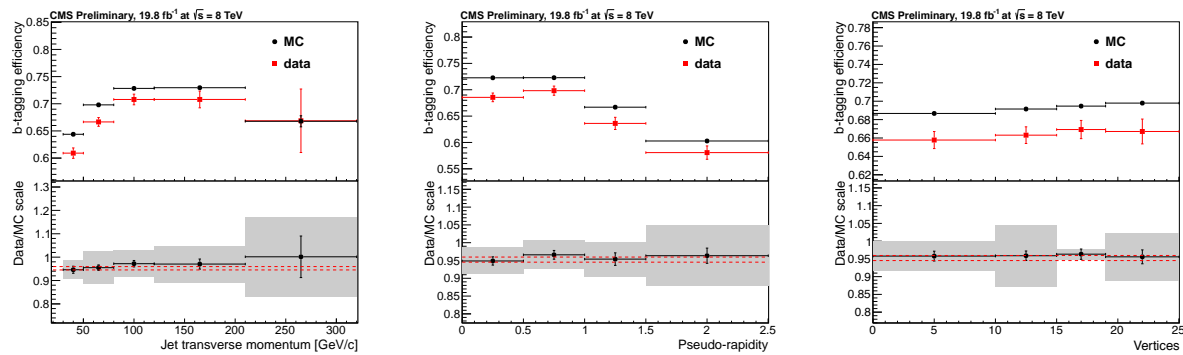


Figure 3.7.: Measured in $t\bar{t} \rightarrow$ di-lepton events using the CSVM tagger: (upper panels) b-tagging efficiencies and (lower panels) data/MC scale factor SF_b as a function of (left) jet p_T , (middle) jet $|\eta|$ and (right) number of primary vertices. In the lower panels, the grey filled areas represent the total statistical and systematic uncertainties, whereas the dotted lines are the average SF_b values within statistical uncertainties.

The measurement of the misidentification probability for light-parton jets relies on the inversion of tagging algorithms, selecting non-b jets using the same variables and techniques used in benchmarking the b-tagging efficiency. The scale factors (SF_s) to be applied to MC are shown in Figure 3.8 for the CSVM tagger.

3.4. Triggering System

With bunch crossings separated by just 25 ns, the rate at which data from all collisions would have to be written out and processed would be unfeasible. A two-tiered triggering system is applied at CMS in order to cope with the high collision rate of protons. The CMS trigger is designed to use limited information from each event to determine whether to record the event, reducing the rate of data taking to manageable levels whilst ensuring a high efficiency of interesting physics object events are selected.

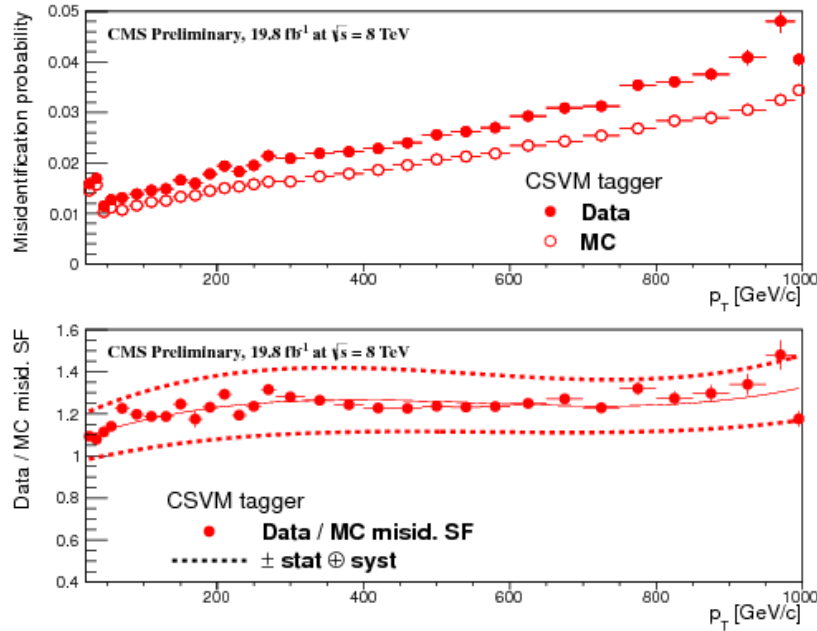


Figure 3.8.: For the **CSVM** tagging criterion: (top) misidentification probability in data (filled circles) and simulation (open circles); (bottom) scale factor for the misidentification probability. The last p_T bin in each plot includes all jets with $p_T > 1000$ GeV. The solid curve is the result of a polynomial fit to the data points. The dashed curves represent the overall statistical and systematic uncertainties on the measurements.

816 The **L1** is a pipelined, dead-timeless system based on custom-built electronics [66],
 817 and is a combination of several sub systems which is shown pictorially in Figure 3.9. The
 818 L1 system is covered in more detail within the following section along with a description
 819 of the service work undertaken by the author to benchmark the performance of the L1
 820 calorimeter trigger during the 2012 8 TeV run period.

821 The Higher Level Trigger (**HLT**) is a large farm of commercial computers [67]. The
 822 **HLT** processes events with software reconstruction algorithms that are more detailed,
 823 giving performance more similar to the reconstruction used offline. The **HLT** reduces
 824 the event rate written to disk by a factor of ~ 500 (~ 200 Hz). The recorded events are
 825 transferred from **CMS** to the **CERN** computing centre, where event reconstruction is
 826 performed, and then distributed to **CMS** computing sites around the globe for storage
 827 and analysis.

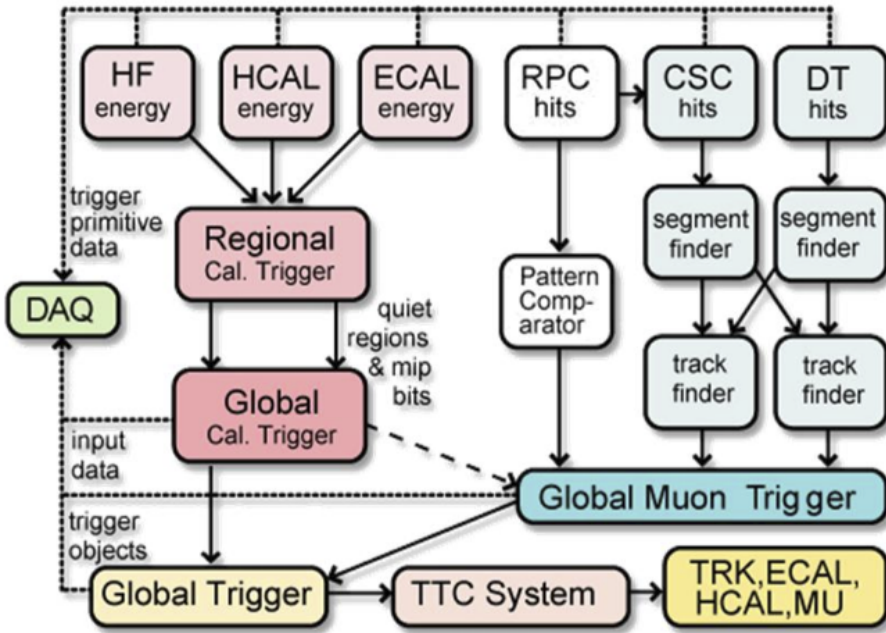


Figure 3.9.: The CMS L1 Trigger system.

3.4.1. The Level-1 Trigger

The L1 trigger reduces the rate of events collected from 40 MHz to ~ 100 kHz using information from the calorimeters and muon chambers, but not the tracker. A tree system of triggers is used to decide whether to pass on an event to the HLT for further reconstruction. Firstly the calorimeter and muon event information is kept separate, with local reconstruction of objects ($\mu, e, \gamma, \text{jets}$) performed by the Regional Calorimeter Trigger (RCT) and Regional Muon Trigger (RMT) respectively. The RCT generates up to 72 isolated and non-isolated electromagnetic objects. These are sorted by rank, which is equivalent to transverse energy E_T , with the four highest ranked electromagnetic objects being passed via the Global Calorimeter Trigger (GCT) and Global MuonTrigger (GMT) to the Global Trigger (GT).

In the L1 GCT, coarse measurements of the energy deposited in the electromagnetic and hadronic calorimeters are combined and by using sophisticated algorithms the following physics objects are formed:

- isolated and non-isolated electromagnetic objects (e and γ);
- hadronic jets in the central and forward sections of the hadronic calorimeters;

- 844 • hadronically decaying tau leptons;
- 845 • total transverse energy (E_T), the scalar sum of the energy measured at L1, and
846 missing transverse energy (\cancel{E}_T), defined as the vector sum of the energy of L1
847 objects;
- 848 • total transverse jet energy (H_T), the scalar sum of the energy of all L1 jet objects,
849 and missing transverse jet energy (\cancel{H}_T), defined as the vector sum of the energy of
850 L1 jets, are calculated from uncorrected L1 jets.

851 In addition quantities suitable for triggering minimum bias events, forward physics and
852 beam background events are calculated. Additionally relevant muon isolation information
853 is also passed on to the **GMT** for decisions involving the muon triggers where it is
854 combined with information from across the three muon sub-systems. The resultant final
855 accept/reject decision at **L1** is then performed by the **GT** based on the objects received
856 from the **GCT** and **GMT** (e/γ , μ , jets, E_T , \cancel{E}_T , H_T).

857 The L1 trigger is therefore of upmost importance to the functioning of the detector.
858 Without a high-performing trigger and a good understanding of it's performance, there
859 would be no data to analyse. Observations of how the L1 trigger performance is affected
860 by changing **LHC** running conditions over the 2012 run period and also the introduction
861 of a jet seed threshold to the L1 jet trigger algorithm is presented in the following Sections
862 (3.4.2 - 3.4.6).

863 3.4.2. L1 Trigger Jet Algorithm

864 The L1 jet trigger uses the transverse energy sums computed in the calorimeter (both
865 hadronic and electromagnetic) trigger regions. Each region consists of 4×4 trigger tower
866 windows, spanning a region of $\Delta\eta \times \Delta\phi = 0.087 \times 0.087$ in pseudorapidity-azimuth. The
867 jet trigger uses a 3×3 calorimeter region (112 trigger towers) sliding window technique
868 which spans the full (η, ϕ) coverage of the **CMS** calorimeter as shown in Figure 3.10.

869 In forming a L1 jet is it required that the central region to be higher than the eight
870 neighbouring regions $E_{T\text{central}} > E_{T\text{surround}}$. Additionally a minimum threshold of 5 GeV
871 on $E_{T\text{central}}$ was introduced during the 2012 run period to suppress noise from pile-up,
872 the effects of which are shown in Section (3.4.4).

873 The L1 jets are characterised by the E_T , summed over the 3×3 calorimeter regions,
874 which corresponds to 12×12 trigger towers in barrel and endcap or 3×3 larger **HF**

875 towers in the **HF**. The ϕ size of the jet window is the same everywhere, whilst the η
876 binning gets somewhat larger at high η due to calorimeter and trigger tower segmentation.
877 The jets are labelled by (η, ϕ) indexes of the central calorimeter region.

878 Jets with $|\eta| > 3.0$ are classified as forward jets, whereas those with $|\eta| < 3.0$ are
879 classified as central. The four highest energy central, forward and τ jets in the calorimeter
880 are passed through Look Up Table (**LUT**)'s, which apply a programmable η -dependent
881 jet energy scale correction. These are then used to make L1 trigger decisions.

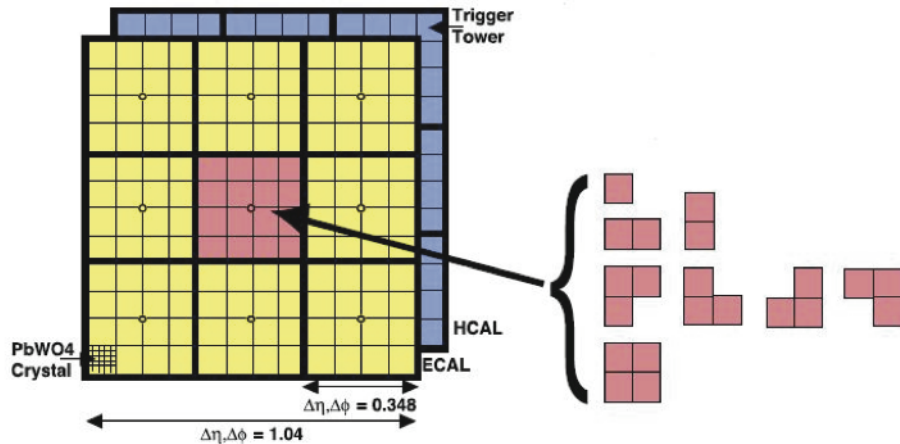


Figure 3.10.: Illustration of the Level-1 jet finding algorithm.

882 The performance of the L1 jets is evaluated with respect to offline jets, which are
883 taken from the standard Calo jet and the PF jet reconstruction algorithms of **CMS**.
884 Jets are corrected for pile-up and detector effects as described in [3.3.1](#). A moderate
885 level of noise rejection is applied to the offline jets by selecting jets passing the “loose
886 identification criteria for both Calo and PF. These criteria are summarised in Appendix
887 ([A.1](#)).

888 3.4.3. Measuring L1 Jet Trigger Efficiencies

889 The L1 jet efficiency is defined as the fraction of leading offline jets which were matched
890 with a L1 tau or central jet above a certain trigger threshold, divided by all the leading
891 offline jets in the event. This quantity is then plotted as a function of the offline jet E_T ,
892 η and ϕ .

893 The efficiency is determined by matching the L1 and reconstructed offline jets spatially
894 in $\eta - \phi$ space. This is done by calculating the minimum separation in ΔR between the

895 highest offline reconstructed jet in E_T ($E_T > 10$ GeV, $|\eta| < 3$) and any L1 jet. A jet will
 896 be matched if this value is found to be < 0.5 . Should more than one jet satisfy this, the
 897 jet closest in ΔR is taken as the matched jet. The matching efficiency is close to 100%,
 898 above ? 30(45) GeV for run 2012B(C) data (see Appendix (??)).

899 Each efficiency curve is fitted with a function which is the cumulative distribution
 900 function of an Exponentially Modified Gaussian (EMG) distribution:

$$901 \quad f(x; \mu, \sigma, \lambda) = \frac{\lambda}{2} \cdot e^{\frac{\lambda}{2}(2\mu + \lambda\sigma^2 - 2x)} \cdot \text{erfc}\left(\frac{\mu + \lambda\sigma^2 - x}{\sqrt{2}\sigma}\right) \quad (3.3)$$

where erfc is the complementary error function defined as:

$$\text{erfc}(x) = 1 - \text{erf}(x) = \frac{2}{\sqrt{\pi}} \int_x^\infty e^{-t^2} dt.$$

902 In this functional form, the parameter μ determines the point of 50% of the plateau
 903 efficiency and the σ gives the resolution. This parametrisation is used to benchmark
 904 the efficiency at the plateau, the turn-on points and resolution for each L1 Jet trigger.
 905 The choice of function is purely empirical. Previous studies used the error function
 906 alone, which described the data well at high threshold values but could not describe the
 907 efficiencies well at lower thresholds [68].

908 The efficiency turn-on curves for various L1 jet thresholds are evaluated as a function
 909 of the offline reconstructed jet E_T for central jets with $|\eta| < 3$. These are measured using
 910 single isolated μ triggers which have high statistics, and are orthogonal and therefore
 911 unbiased to the hadronic triggers under study. The efficiency is calculated with respect to
 912 offline Calo and PF Jets in Figure 3.11. Table 3.1 shows the values of these parameters,
 913 calculated for three example L1 single jet triggers taken from 2012 8 TeV data.

914 The results from the L1 single jet triggers shows good performance for both Calo and
 915 PF jets. A better resolution for Calo jets with respect to L1 jets quantities is observed.
 916 This effect is due to Calo jet reconstruction using the same detector systems as in L1 jets,
 917 whereas with PF jet construction using tracker and muon information, a more smeared
 918 resolution when compared to L1 is expected.

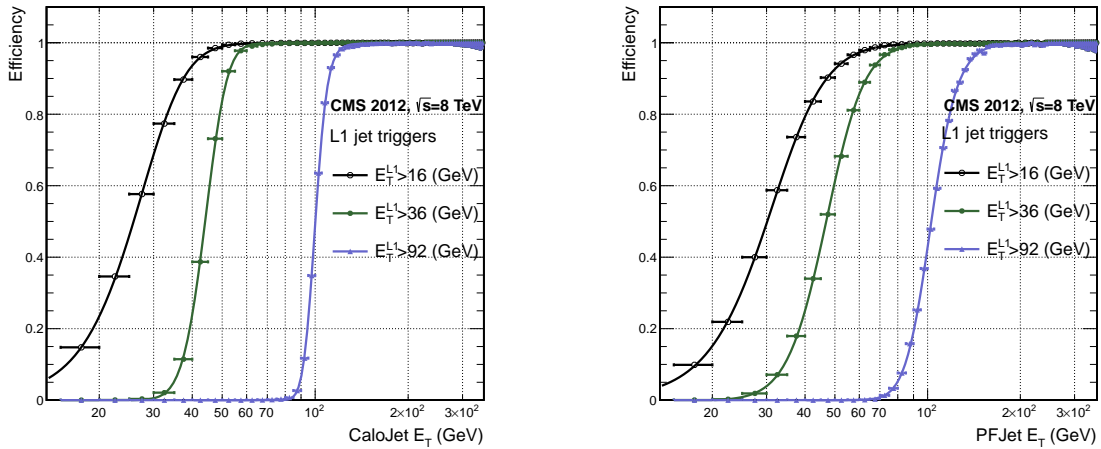


Figure 3.11.: L1 jet efficiency turn-on curves as a function of the offline CaloJet E_T (left) and PFJet E_T (right), measured in 2012 Run Period C data and collected with an isolated single μ data sample.

Trigger	Calo		PF	
	μ	σ	μ	σ
L1_SingleJet16	21.09 ± 0.03	7.01 ± 0.02	22.17 ± 0.04	7.83 ± 0.03
L1_SingleJet36	41.15 ± 0.05	5.11 ± 0.02	39.16 ± 0.06	8.04 ± 0.03
L1_SingleJet92	95.36 ± 0.13	5.62 ± 0.03	90.85 ± 0.19	11.30 ± 0.10

Table 3.1.: Results of a cumulative EMG function fit to the turn-on curves for L1 single jet triggers in run 2012 Run Period C, measured in an isolated μ data sample. The turn-on point, μ , and resolution, σ , of the L1 jet triggers are measured with respect to offline Calo Jets (left) and PF Jets (right).

3.4.4. Effects of the L1 Jet Seed

Between run period B and C of the 2012 data taking period, a jet seed threshold was introduced into the L1 trigger jet algorithm. There was previously no direct requirement made on the energy deposited in the central region. The introduction of a jet seed threshold required that the central region have $E_T \geq 5\text{GeV}$, and was introduced to counteract the effects of high pile up running conditions which create a large number of soft non-collimated jets, that are then added to the jets from the primary interaction or other soft jets from other secondary interactions [69]. This in turn causes a large increase in trigger rate due to the increase in the likelihood that the event causes the L1 trigger to fire. This was implemented to maintain trigger thresholds by cutting the rate of events recorded without significant reduction in the efficiency of physics events of interest.

930 The effect of the introduction of this jet seed threshold between these two run periods
 931 is benchmarked through a comparison of the efficiency of the L1 jet triggers with respect
 932 to offline Calo jets shown in Figure 3.12, and the L1 H_T trigger efficiency in Figure 3.14
 933 which is compared to offline H_T constructed from Calo jets with $E_T \geq 40\text{GeV}$.

934 To negate any effects from different pile-up conditions in the run periods, the efficiencies
 935 are measured in events which contain between 15 and 20 primary vertices as defined in
 936 Appendix (A.2).

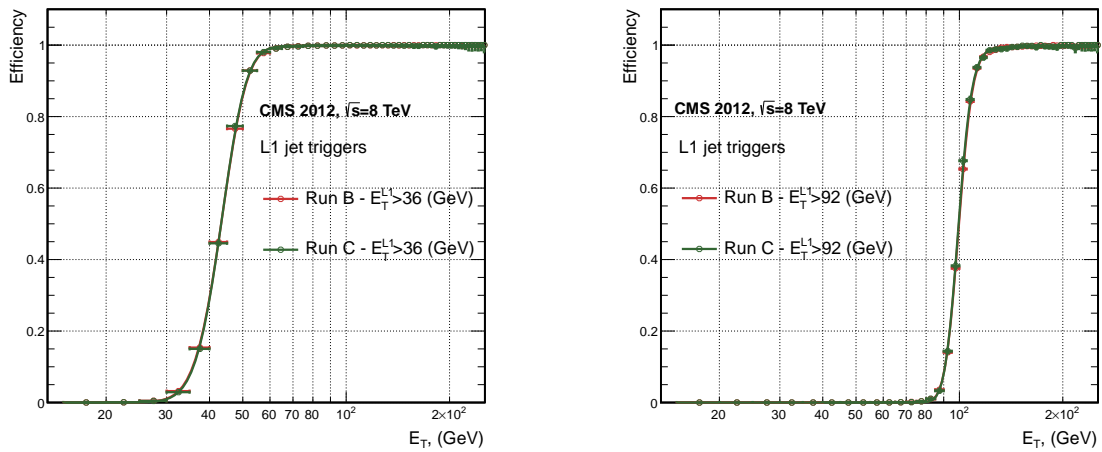


Figure 3.12.: L1 jet efficiency turn-on curves as a function of the offline CaloJet E_T , measured for the L1 SingleJet 36 and 92 trigger in 2012 run period B and C collected with an isolated single μ' sample.

937 It can be seen that the performance of the $E_T > 36, 92$ single jet are almost identical,
 938 with the jet seed having no measurable effect on these triggers as shown in Table 3.2 .

Trigger	2012B		2012C	
	μ	σ	μ	σ
L1_SingleJet36	40.29 ± 0.04	5.34 ± 0.02	40.29 ± 0.11	5.21 ± 0.05
L1_SingleJet92	94.99 ± 0.09	5.93 ± 0.06	94.82 ± 0.29	5.74 ± 0.18

Table 3.2.: Results of a cumulative EMG function fit to the turn-on curves for L1 single jet triggers in the 2012 run period B and C, preselected on an isolated muon trigger. The turn-on point μ and resolution σ of the L1 jet triggers are measured with respect to offline Calo Jets in run B (left) and run C (right).

939 For the H_T triggers, a large increase in rate during high pile-up conditions is expected.
 940 This is due to the low energy threshold required for a jet to be added to the L1 H_T sum,

which is compiled from all uncorrected L1 jets formed in the RCT. The introduction of the jet seed threshold removes the creation of many of these soft low E_T jets, thus lowering the H_T calculation at L1. The effect on the trigger cross section for L1 H_T 150 trigger can be seen in Figure 3.13.

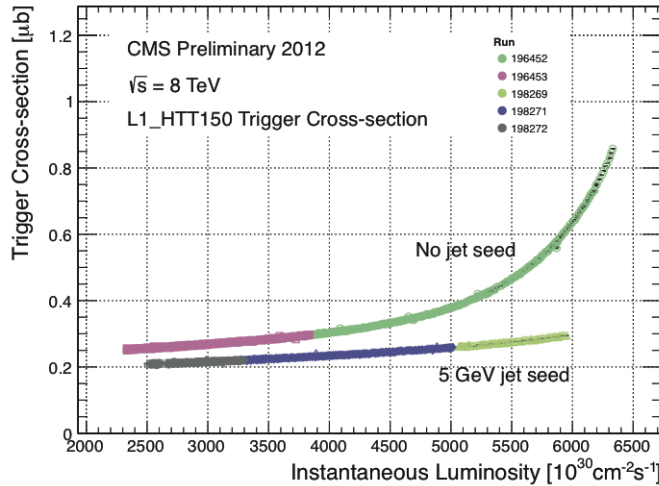


Figure 3.13.: Trigger cross section for the L1HTT150 trigger path. Showing that a 5 GeV jet seed threshold dramatically reduces the dependance of cross section on the instantaneous luminosity for L1 H_T triggers [70].

Different behaviours for the trigger turn ons between these run periods are therefore expected. The turn on point is observed to shift to higher H_T values after the introduction of the jet seed threshold, whilst having a sharper resolution due to less pile-up jets being included the H_T sum, the results are shown in Table 3.3.

Trigger	2012B		2012C	
	μ	σ	μ	σ
L1 HT-100	157.5 ± 0.08	32.9 ± 0.08	169.8 ± 0.08	28.7 ± 0.03
L1 H1-150	230.9 ± 0.02	37.3 ± 0.01	246.4 ± 0.16	31.8 ± 0.05

Table 3.3.: Results of a cumulative EMG function fit to the turn-on curves for H_T in run 2012 B and C, preselected on an isolated single μ trigger. The turn-on point μ , resolution σ of the L1 H_T triggers are measured with respect to offline H_T formed from CaloJets with a $E_T \geq 40$ in run period B (left) and C (right).

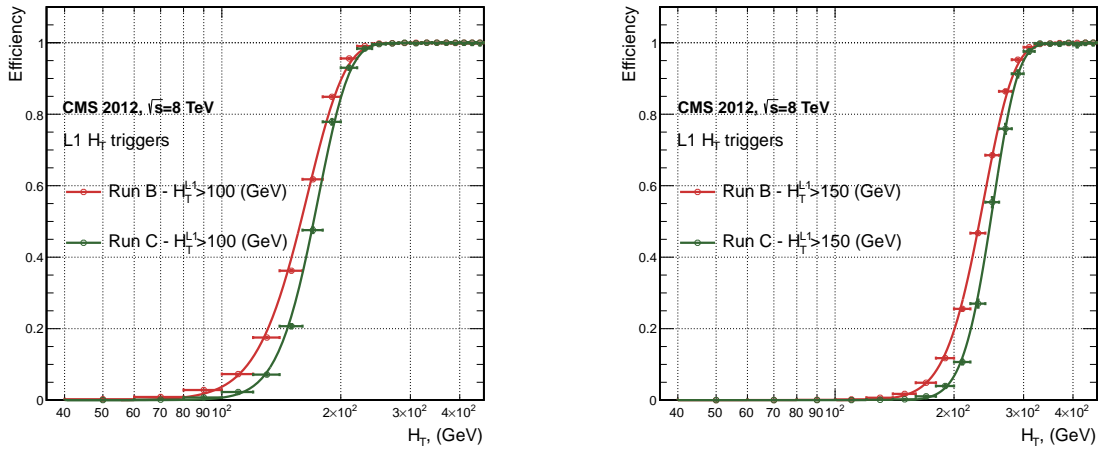


Figure 3.14.: L1 H_T efficiency turn-on curves as a function of the offline CaloJet H_T , measured for the L1 H_T 100 and 150 trigger during the run 2012 B and C collected using an isolated single μ triggered sample.

949 3.4.5. Robustness of L1 Jet Performance against Pile-up

950 The performance of the L1 single jet triggers is evaluated in different pile-up conditions
 951 to benchmark any dependence on pile-up. Three different pile-up bins of 0-10, 10-20 and
 952 >20 vertices are defined, reflecting the low, medium and high pile-up running conditions
 953 at CMS in 2012. This is benchmarked relative to Calo and PF jets for the run 2012 C
 954 period where the jet seed threshold is applied, with L1 single jet thresholds of 16, 36 and
 955 92 GeV, shown in Figure 3.15. The results of fits to these efficiency turn-on curves are
 956 given in Table 3.4 and Table 3.5 for Calo and PF jets respectively.

Vertices	0-10		11-20		> 20	
	μ	σ	μ	σ	μ	σ
L1_SingleJet16	19.9 ± 0.1	6.1 ± 0.3	20.8 ± 0.1	6.5 ± 0.1	22.3 ± 0.2	7.5 ± 0.1
L1_SingleJet36	41.8 ± 0.1	4.6 ± 0.1	40.9 ± 0.1	5.1 ± 0.1	40.6 ± 0.6	5.9 ± 0.2
L1_SingleJet92	95.9 ± 0.2	5.4 ± 0.1	95.2 ± 0.2	5.6 ± 0.1	94.5 ± 0.6	6.2 ± 0.3

Table 3.4.: Results of a cumulative EMG function fit to the efficiency turn-on curves for L1 single jet triggers in the 2012 run period C, measured from isolated μ triggered data. The turn-on point, μ , and resolution, σ , of the L1 jet triggers are measured with respect to offline Calo jets in low (left), medium (middle) and high (right) pile-up conditions.

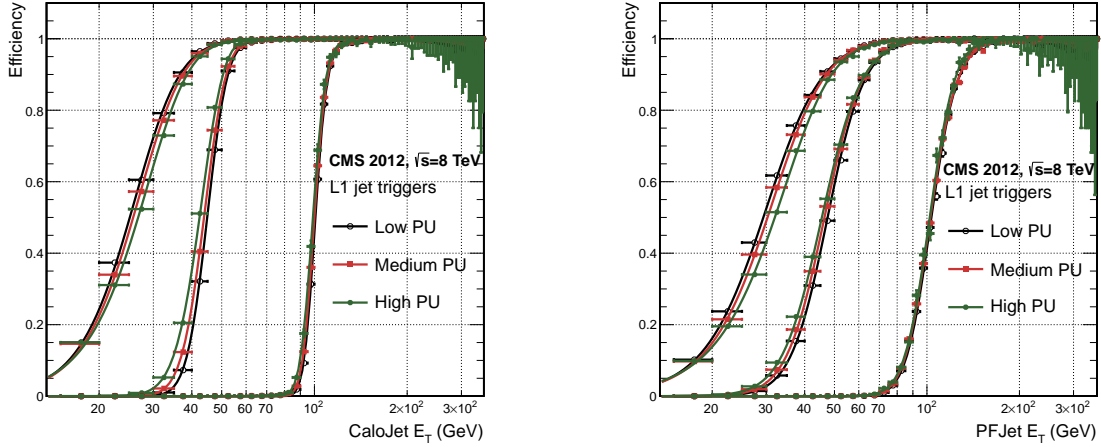


Figure 3.15.: L1 jet efficiency turn-on curves as a function of the leading offline E_T Calo (left) and PF (right) jet, for low, medium and high pile-up conditions.

Vertices	0-10		11-20		> 20	
	μ	σ	μ	σ	μ	σ
L1_SingleJet16	21.1 ± 0.1	7.16 ± 0.05	22.34 ± 0.1	7.9 ± 0.1	24.6 ± 0.2	9.5 ± 0.1
L1_SingleJet36	39.6 ± 0.1	7.4 ± 0.1	38.4 ± 0.1	7.4 ± 0.1	37.1 ± 0.2	7.5 ± 0.1
L1_SingleJet92	91.6 ± 0.3	11.3 ± 0.2	90.4 ± 0.3	11.2 ± 0.1	92.0 ± 0.9	12.1 ± 0.4

Table 3.5.: Results of a cumulative EMG function fit to the efficiency turn-on curves for Level-1 single jet triggers in the 2012 run period C, measured from isolated μ triggered data. The turn-on point, μ , and resolution, σ , of the L1 jet triggers are measured with respect to offline PF jets in low (left), medium (middle) and high (right) pile-up conditions.

957 No significant drop in efficiency is observed in the presence of a high number of
 958 primary vertices. The increase in hadronic activity in higher pile-up conditions, combined
 959 with the absence of pile-up subtraction for L1 jets, results in the expected observation of
 960 a decrease in the μ value of the efficiency turn-ons as a function of pile-up, while the
 961 resolution, σ of the turn-ons are found to gradually worsen as expected with increasing
 962 pile-up.

963 These features are further emphasised when shown as a function of

$$\frac{(L1 E_T - \text{Offline } E_T)}{\text{Offline } E_T} \quad (3.4)$$

in bins of matched leading offline jet E_T , of which the individual fits can be found in Appendix (B.2). Each of these distributions are fitted with an EMG function as defined in Equation (3.3).

The μ , σ and λ values extracted for the low, medium and high pile-up conditions are shown for Calo and PF jets in Figure 3.16 and Figure 3.17 respectively. The central value of $\frac{(L1 E_T - \text{Offline } E_T)}{\text{Offline } E_T}$ is observed to increases as a function of jet E_T , whilst the resolution is also observed to improve at higher offline jet E_T .

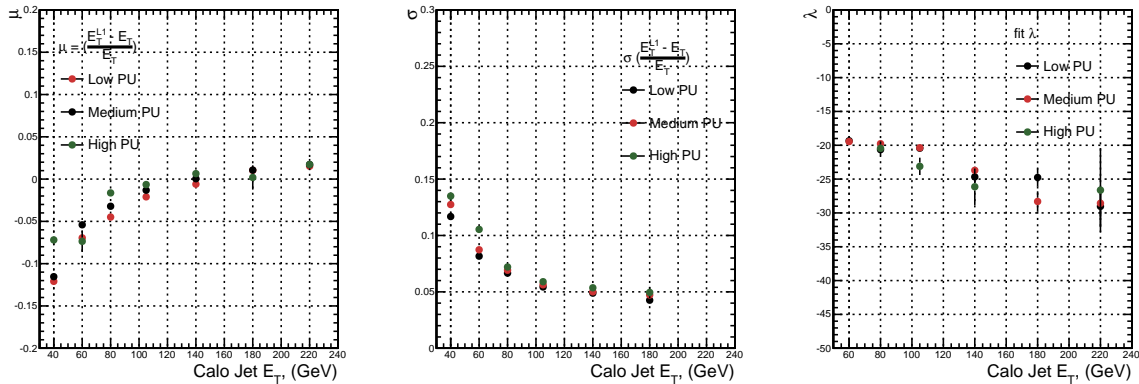


Figure 3.16.: Fit values from an EMG function fitted to the resolution plots of leading Calo jet E_T measured as a function of $\frac{(L1 E_T - \text{Offline } E_T)}{\text{Offline } E_T}$ for low, medium and high pile-up conditions. The plots show the mean μ (left), resolution σ (middle) of the Gaussian as well as the decay term λ (right) of the exponential.

The resolution of other L1 energy sum quantities, H_T , \not{E}_T and $\sum E_T$ parameterised as in Equation (3.4), can be found in Appendix (B.3). The same behaviour observed for the single jet triggers is also found for these quantities, where in the presence of higher pile-up the μ values are shifted to higher values, with a worsening resolution, σ again due to the increase in soft pile-up jets and the absence of pile-up subtraction at L1.

3.4.6. Summary

The performance of the CMS Level-1 Trigger has been studied and evaluated for jets and energy sum quantities using data collected during the 2012 LHC 8TeV run. These studies include the effect of introduction of a 5 GeV jet seed threshold into the jet algorithm configuration, the purpose of which is to mitigate the effects of pile-up on the rate of L1 triggers whilst not adversely affecting the efficiency of these triggers. No significant

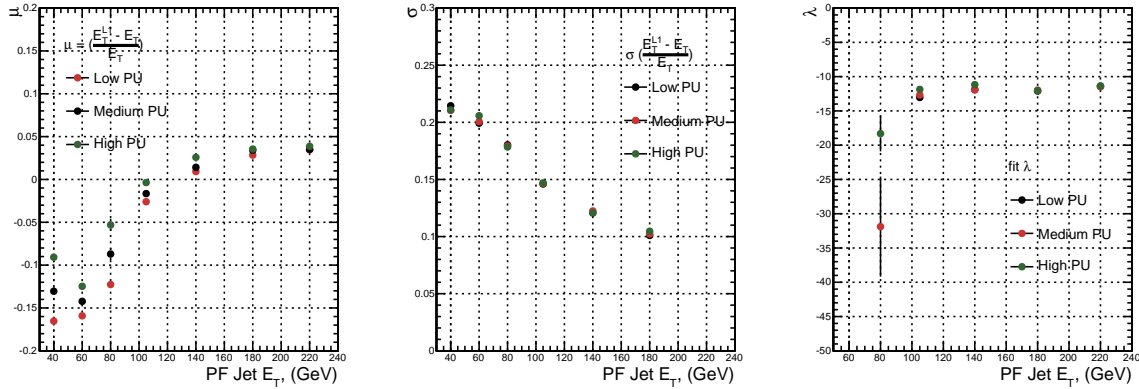


Figure 3.17.: Fit values from an **EMG** function fitted to the resolution plots of leading PF jet E_T measured as a function of $\frac{(L1 E_T - \text{Offline } E_T)}{\text{Offline } E_T}$ for low and medium pile-up conditions. The plots show the mean μ (left), resolution σ (middle) of the Gaussian as well as the decay term λ (right) of the exponential.

982 change in performance is observed with this change and good performance is observed
 983 for a range of L1 quantities.

Chapter 4.

984 SUSY searches in Hadronic Final 985 States

986 In this chapter a model independent search for SUSY in hadronic final states with \cancel{E}_T
987 using the α_T variable and b-quark multiplicity is introduced and described in detail. The
988 results presented are based on a data sample of pp collisions collected in 2012 at $\sqrt{s} = 8$
989 TeV, corresponding to an integrate luminosity of $11.7 \pm 0.5 \text{ fb}^{-1}$.

990 The kinematic variable α_T is motivated as a variable to provide strong rejections
991 of QCD backgrounds, whilst maintaining sensitivity to possible a SUSY signal within
992 Section (4.1). The search and trigger strategy in addition to the event reconstruction
993 and selection are outlined within Sections (4.2-4.2.2).

994 The method in which the SM background is estimated using an analytical technique
995 to improve statistical precision at higher b-tag multiplicities is detailed within Section
996 (4.4), with a discussion on the impact of b-tagging and mis-tagging scale factors between
997 data and MC on any background predictions. Finally a description of the formulation of
998 appropriate systematic uncertainties applied to the background predictions to account for
999 theoretical uncertainties and limitations in the simulation modelling of event kinematics
1000 and instrumental effects is covered in Section (4.5).

1001 In addition to the α_T search, a complimentary technique is discussed as a means to
1002 predict the distribution of 3 and 4 reconstructed b-quark jets in an event in Section
1003 (4.6). The recent discovery of the Higgs boson has made third-generation “Natural SUSY”
1004 models attractive, given that light top and bottom squarks are a candidate to stabilise
1005 divergent loop corrections to the Higgs boson mass.

1006 Using the α_T search as a base, a simple templated fit is employed to estimate the
 1007 **SM** background in higher b-tag multiplicities (3-4) from a region of a low number
 1008 of reconstructed b-jets (0-2). The predictions using this technique are first tested in
 1009 simulation before being compared to the **SM** background predictions obtained from the
 1010 α_T search.

1011 The experimental reach of the analysis discussed within this thesis is interpreted in
 1012 two classes of **SMS** models, the topologies of which are detailed in Section (2.4.1). The
 1013 **SMS** models considered in this analysis are summaries in Table 4.1. For each model, the
 1014 **LSP** is assumed to be the lightest neutralino.

1015 Within Table 4.1 is also defined reference points, parameterised in terms of parent
 1016 gluino/squark and **LSP** sparticle masses, m_{parent} and m_{LSP} , respectively, which are used
 1017 within the following two chapters to demonstrate potential yields within the signal region
 1018 of the search. The masses are chosen to reflect parameter space which is within the
 1019 expect sensitivity reach of the search.

Model	Production/decay mode	Reference model	
		m_{parent}	m_{LSP}
G1 (T1)	$pp \rightarrow \tilde{g}\tilde{g}^* \rightarrow q\bar{q}\tilde{\chi}_1^0 q\bar{q}\tilde{\chi}_1^0$	700	300
G2 (T1bb)	$pp \rightarrow \tilde{g}\tilde{g}^* \rightarrow b\bar{b}\tilde{\chi}_1^0 b\bar{b}\tilde{\chi}_1^0$	900	500
G3 (T1tt)	$pp \rightarrow \tilde{g}\tilde{g}^* \rightarrow t\bar{t}\tilde{\chi}_1^0 t\bar{t}\tilde{\chi}_1^0$	850	250
D1 (T2)	$pp \rightarrow \tilde{q}\tilde{q}^* \rightarrow q\tilde{\chi}_1^0 \bar{q}\tilde{\chi}_1^0$	600	250
D2 (T2bb)	$pp \rightarrow \tilde{b}\tilde{b}^* \rightarrow b\tilde{\chi}_1^0 \bar{b}\tilde{\chi}_1^0$	500	150
D3 (T2tt)	$pp \rightarrow \tilde{t}\tilde{t}^* \rightarrow t\tilde{\chi}_1^0 \bar{t}\tilde{\chi}_1^0$	400	0

Table 4.1.: A summary of the **SMS** models interpreted in this analysis, involving both direct (D) and gluino-induced (G) production of squarks and their decays. Reference models are also defined in terms of parent and **LSP** sparticle mass

1020 4.1. An introduction to the α_T search

1021 The experimental signature of **SUSY** signal in the hadronic channel would manifest as a
 1022 final state containing energetic jets and \cancel{E}_T . The search focuses on topologies where new
 1023 heavy supersymmetric, R-parity conserving particles are pair-produced in pp collisions.
 1024 These particles decaying to a **LSP** escape the detector undetected, leading to significant
 1025 missing energy and missing hadronic transverse energy,

$$\mathcal{H}_T = \left| \sum_{i=1}^n p_T^{jet_i} \right|, \quad (4.1)$$

1026 defined as the vector sum of the transverse energies of jets selected in an event.
1027 Energetic jets produced in the decay of these supersymmetric particles also can produce
1028 significant visible transverse energy,

$$H_T = \sum_{i=1}^n E_T^{jet_i}, \quad (4.2)$$

1029 defined as the scalar sum of the transverse energies of jets selected in an event.

1030 A search within this channel is greatly complicated in a hadron collider environment,
1031 where the overwhelming background comes from inherently balanced multi-jet (“QCD”)
1032 events which are produced with an extremely large cross section as demonstrated within
1033 Figure 4.1. \cancel{E}_T can appear in such events with a substantial mis-measurement of jet
1034 energy or missed objects due to detector miscalibration or noise effects.

1035 Additional **SM** background from **EWK** processes with genuine \cancel{E}_T from escaping
1036 neutrinos comprise the irreducible background within this search and come mainly from:

- 1037 • $Z \rightarrow \nu\bar{\nu}$ + jets,
- 1038 • $W \rightarrow l\nu$ + jets in which a lepton falls outside of detector acceptance, or the lepton
1039 decays hadronically $\tau \rightarrow \text{had}$,
- 1040 • $t\bar{t}$ with at least one leptonic W decay,
- 1041 • small background contributions from DY, single top and Diboson (WW,ZZ,WZ)
1042 processes.

1043 The search is designed to have a strong separation between events with genuine and
1044 “fake” \cancel{E}_T which is achieved primarily through the dimensionless kinematic variable, α_T
1045 [71][72].

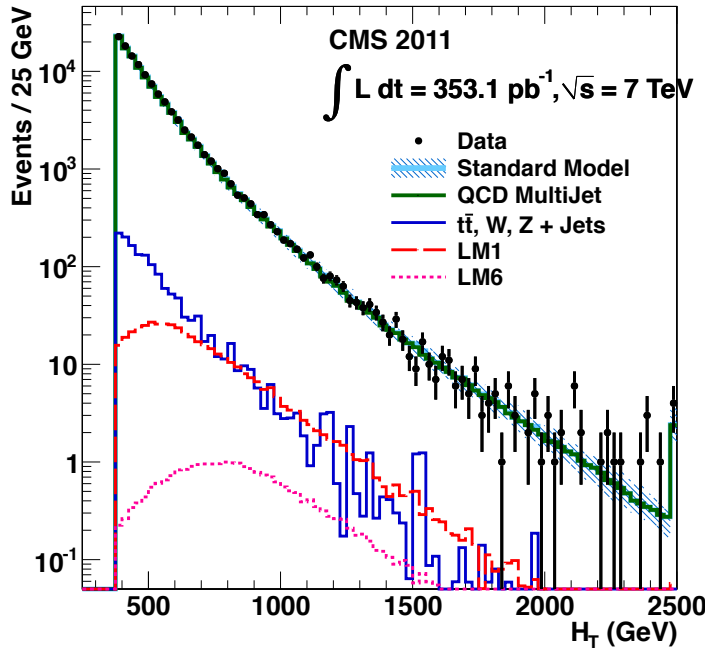


Figure 4.1.: Reconstructed offline H_T for 11.7fb^{-1} of data after a basic pre-selection. Sample is collected from prescaled H_T triggers. Overlaid are expectations from MC simulation of EWK processes as well as a reference signal model (labelled D2 from Table 4.1).

1046 4.1.1. The α_T variable

1047 For a perfectly measured di-jet QCD event, conservation laws dictate that they must be
 1048 produced back-to-back and of equal magnitude. However in di-jet events with real \cancel{E}_T , both of these jets are produced independently of one another, depicted in Figure 4.2.

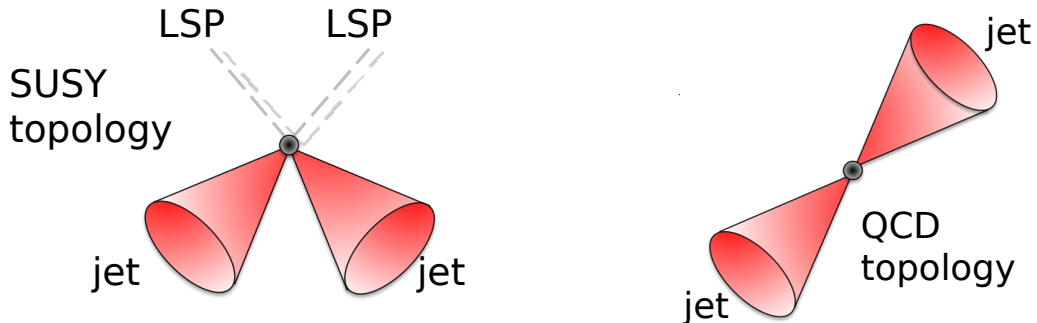


Figure 4.2.: The event topologies of background QCD dijet events (right) and a generic SUSY signature with genuine \cancel{E}_T (left).

1050 Exploiting this feature leads to the formulation of α_T in di-jet systems defined as,

$$\alpha_T = \frac{E_T^{j2}}{M_T}, \quad (4.3)$$

1051 where E_T^{j2} is the transverse energy of the least energetic of the two jets and M_T
1052 defined as:

$$M_T = \sqrt{\left(\sum_{i=1}^2 E_T^{ji}\right)^2 - \left(\sum_{i=1}^2 p_x^{ji}\right)^2 - \left(\sum_{i=1}^2 p_y^{ji}\right)^2} \equiv \sqrt{H_T^2 - \cancel{H}_T^2}. \quad (4.4)$$

1053 A perfectly balanced di-jet event i.e. $E_T^{j1} = E_T^{j2}$ would give an $\alpha_T = 0.5$, where as
1054 events with jets which are not back-to-back, for example in events in which a W or Z
1055 recoils off a system of jets, α_T can achieve values in excess of 0.5.

1056 α_T can be extended to apply to any arbitrary number of jets, undertaken by modelling
1057 a system of n jets as a di-jet system, through the formation of two pseudo-jets [73].
1058 The two pseudo-jets are built by merging the jets present in the event such that the 2
1059 pseudo-jets are chosen to be as balanced as possible, i.e the $\Delta H_T \equiv |E_T^{pj1} - E_T^{pj2}|$ is
1060 minimised between the two pseudo jets. Using Equation (4.4), α_T can be rewritten as,

$$\alpha_T = \frac{1}{2} \frac{H_T - \Delta H_T}{\sqrt{H_T^2 - \cancel{H}_T^2}} = \frac{1}{2} \frac{1 - \Delta H_T/H_T}{\sqrt{1 - (\cancel{H}_T/H_T)^2}}. \quad (4.5)$$

1061 The distribution of α_T for the two jet categories used within this analysis, 2,3 and
1062 ≥ 4 jets, is shown in the Figure 4.3, demonstrating the ability of the α_T variable to
1063 discriminate between multi jet events and EWK processes with genuine \cancel{E}_T in the final
1064 state.

1065 The α_T requirement used within the search is chosen to be $\alpha_T > 0.55$ to ensure
1066 that the QCD multijet background is negligible even in the presence of moderate jet
1067 mis-measurement. There still remains other effects which can cause multijet events to
1068 artificially have a large α_T value, which are discussed in detail in Section (4.2.2).

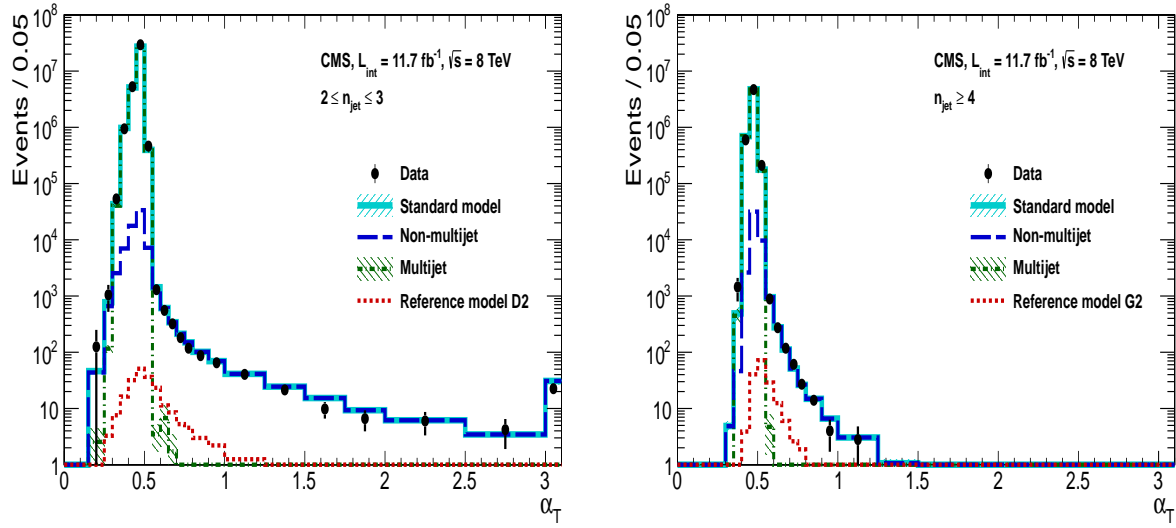


Figure 4.3.: The α_T distributions for the low 2-3 (left) and high ≥ 4 (right) jet multiplicities after a full analysis selection and shown for $H_T > 375$. Data is collected using both prescaled H_T triggers and dedicated α_T triggers for below and above $\alpha_T = 0.55$ respectively. . Expected yields as given by simulation are also shown for multijet events (green dash-dotted line), EWK backgrounds with genuine \cancel{E}_T (blue long-dashed line), the sum of all SM processes (cyan solid line) and the reference signal model D2 (left, red dotted line) or G2 (right, red dotted line).

1069 4.2. Search Strategy

1070 The aim of the analysis presented in this thesis is to identify an excess of events in data
 1071 over the SM background expectation in multi-jet final states and significant \cancel{E}_T . The
 1072 essential suppression of the dominant QCD background for such a search is addressed by
 1073 the α_T variable described in the previous section. For estimation of the remaining EWK
 1074 backgrounds, three independent data control samples are used to predict the different
 1075 processes that compose the background :

- 1076 • $\mu + \text{jets}$ to determine $W + \text{jets}$, $t\bar{t}$ and single top backgrounds,
- 1077 • $\gamma + \text{jets}$ to determine the irreducible $Z \rightarrow \nu\bar{\nu} + \text{jets}$ background,
- 1078 • $\mu\mu + \text{jets}$ to determine the irreducible $Z \rightarrow \nu\bar{\nu} + \text{jets}$ background.

1079 These control samples are chosen to both be rich in specific EWK processes, be free of
 1080 QCD multi-jet events and to also be kinematically similar to the hadronic signal region
 1081 that they are estimating the backgrounds of, see Section (4.2.3).

1082 To remain inclusive to a large range of possible **SUSY** models, the signal region is
1083 binned in the following categories to allow for increased sensitivity in the interpretation
1084 of results for different **SUSY** topologies:

1085 **Sensitivity to a range of SUSY mass splittings**

1086 The hadronic signal region is defined by $H_T > 275$, divided into eight bins in H_T .

- 1087 – Two bins of width 50 GeV in the range $275 < H_T < 375$ GeV,
1088 – five bins of width 100 GeV in the range $375 < H_T < 875$ GeV,
1089 – and a final open bin, $H_T > 875$ GeV.

1090 The choice at low H_T is driven primarily by trigger constraints. The mass difference
1091 between the **LSP** and the particle that it decays from is an important factor in the
1092 amount of hadronic activity in the event.

1093 A large mass splitting will lead to hard high p_T jets which contribute to the H_T
1094 sum. From Figure 4.1 it can be seen that the **SM** background falls sharply at high
1095 H_T values, therefore a large number of H_T bins will lead to easier identification
1096 of such signals. Conversely smaller mass splittings lead to softer jet p_T 's which will
1097 subsequently fall into the lower H_T range.

1098 **Sensitivity to production method of SUSY particles**

1099 The production mechanism of any potential **SUSY** signal can lead to different event
1100 topologies. One such way to discriminate between gluino ($g\tilde{g}$ - “high multiplicity”),
1101 and direct squark ($q\tilde{q}$ - “low multiplicity”) induced production of **SUSY** particles is
1102 realised through the number of reconstructed jets in the final state.

1103 The analysis is thus split into two jet categories : 2-3 jets , ≥ 4 jets to give sensitivity
1104 to both of these mechanisms.

1105 **Sensitivity to “Natural SUSY” via tagging jets from b-quarks**

1106 Jets originating from bottom quarks (b-jets) are identified through vertices that
1107 are displaced with respect to the primary interaction. The algorithm used to tag
1108 b-jets is the Combined Secondary Vertex Medium Working Point (**CSV**) tagger,
1109 described within Section (3.3.2). A cut is placed on the discriminator variable of
1110 > 0.679 , leading to a gluon/light-quark mis-tag rate of 1% and a jet p_T dependant
1111 b-tagging efficiency of 60-70% [64].

Natural **SUSY** models would be characterised through final-state signatures rich in bottom quarks. A search relying on methods to identify jets originating from bottom quarks through b-tagging, will significantly improve the sensitivity to this class of signature.

This is achieved via the binning of events in the signal region according to the number of b-tagged jets reconstructed in each event, in the following: 0,1,2,3, ≥ 4 b-tag categories . In the highest ≥ 4 b-tag category due to a limited number of expected signal and background, just three H_T bins are employed: 275-325 GeV, 325-375 GeV, ≥ 375 GeV.

This characterisation is identically mirrored in all control samples, with the information from all samples and b-tag categories used simultaneously in the likelihood model (see Chapter 5) in order to interpret the results in a coherent and powerful way.

The combination of the H_T , jet multiplicity and b-tag categorisation of the signal region as described above, resultantly leads to 67 different bins in which the analysis is interpreted in, which is depicted in Figure 4.4.

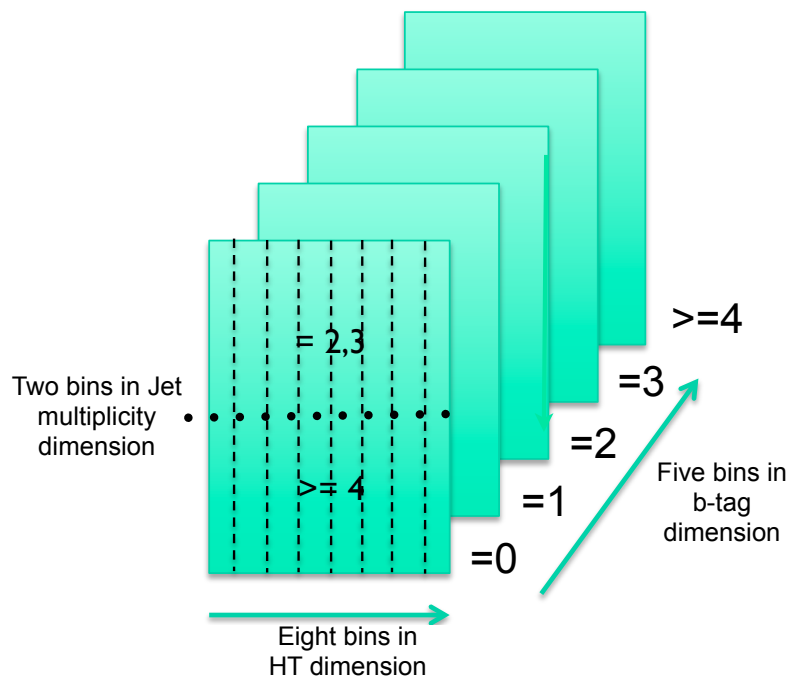


Figure 4.4.: Pictorial depiction of the analysis strategy employed by the α_T search to increase sensitivity to a wide spectra of **SUSY** models.

¹¹²⁸ **4.2.1. Physics Objects**

¹¹²⁹ Jets are reconstructed

¹¹³⁰ Muon id Table 4.2

Model	Production/decay mode	Reference model	
		m_{parent}	m_{LSP}
G1 (T1)	$pp \rightarrow \tilde{g}\tilde{g}^* \rightarrow q\bar{q}\tilde{\chi}_1^0 q\bar{q}\tilde{\chi}_1^0$	700	300

Table 4.2.: Muon Id.

¹¹³¹ Photon id Table 4.3

Model	Production/decay mode	Reference model	
		m_{parent}	m_{LSP}
G1 (T1)	$pp \rightarrow \tilde{g}\tilde{g}^* \rightarrow q\bar{q}\tilde{\chi}_1^0 q\bar{q}\tilde{\chi}_1^0$	700	300

Table 4.3.: Muon Id.

¹¹³² **4.2.2. Event Selection**

¹¹³³ Events are selected...

¹¹³⁴ **4.2.3. Control Sample Definition**

¹¹³⁵ The method used to estimate the background contributions in the hadronic signal region
¹¹³⁶ relies on the use of a Transfer Factor (**TF**). This is determined from MC simulation
¹¹³⁷ in both the control, $N_{MC}^{control}$, and signal, N_{MC}^{signal} , region to transform the observed yield
¹¹³⁸ measured in data for a control sample, $N_{obs}^{control}$, into a background prediction, N_{pred}^{signal} , via
¹¹³⁹ Equation (4.6),

$$N_{pred}^{signal} = \frac{N_{MC}^{signal}}{N_{MC}^{control}} \times N_{obs}^{control}. \quad (4.6)$$

1140 The control samples and the EWK processes they are specifically tuned to select are
1141 defined below:

1142 **The $\mu +$ jets control sample**

1143 Events from $W +$ jets and $t\bar{t}$ processes enter into the hadronic signal sample due to
1144 unidentified leptons from acceptance or threshold effects and hadronic tau decays.
1145 These leptons originate from the decay of high p_T W bosons.

1146 The control samples specifically identifies $W \rightarrow \mu\bar{\nu}$ decays within the same phase-
1147 space of the signal region, where the muon is subsequently ignored in the calculation
1148 of event level variables, i.e. H_T , \mathcal{H}_T , α_T . All kinematic jet-based cuts are identical
1149 to those applied in the hadronic search region detailed in Section (4.2.2), with the
1150 same H_T , jet multiplicity and b-jet multiplicity binning described above.

1151 Muons originating from W boson decays are selected by requiring one tightly
1152 isolated muon defined in Table 4.2, with a $p_T > 10$ GeV and $|\eta| < 2.1$. Additionally
1153 the transverse mass of the W candidate must satisfy $M_T(\mu, \cancel{E}_T) < 30$ GeV (to
1154 suppress QCD multi-jet events). Events which contain a jet overlapping with a
1155 muon $\Delta R(\mu, \text{jet}) < 0.5$ are vetoed to remove events from muons produced as part
1156 of a jet's hadronisation process. Furthermore events containing a second muon
1157 candidate which has failed id, but passed p_T and $|\eta|$ requirements, are checked to
1158 have an invariant mass that satisfies $m_Z = 25 < M_{\mu_1\mu_2} > m_Z + 25$, thus removing
1159 $Z \rightarrow \mu\mu$ contamination.

1160 **The $\mu\mu +$ jets control sample**

1161 The $Z \rightarrow \nu\bar{\nu} +$ jets background enters into the signal region from genuine \cancel{E}_T from
1162 the escaping neutrinos. This background is estimated using two control samples,
1163 the first of which is the $Z \rightarrow \mu\bar{\mu} +$ jets process, which posses identical kinematic
1164 properties, but with different acceptance and branching ratio [1].

1165 Selection criteria are applied to identify two tightly isolated muons as defined
1166 in Table 4.2, with the same acceptance requirements of the $\mu +$ jets selection.
1167 Both muons are ignored for the purpose of the calculation of event level variables.
1168 Kinematic jet-based cuts and phase space binning identical to the hadronic search
1169 region are also applied.

1170 In order to specifically select two muons both originating from a single Z boson
1171 decay, the invariant mass of the two muons must satisfy $m_Z - 25 > M_{\mu_1\mu_2} < m_Z$

1172 + 25. Additionally events are vetoed if containing a jet overlapping with a muon
1173 $\Delta R(\mu, \text{jet}) < 0.5$.

1174 The $\mu\mu + \text{jets}$ sample is used to make predictions in the signal region in the two
1175 lowest H_T bins, providing coverage where the $\gamma + \text{jets}$ sample is unable to, due to
1176 trigger requirements. In higher H_T bins, the higher statistics of the $\gamma + \text{jets}$ sample
1177 is instead used to determine the $Z \rightarrow \nu\bar{\nu}$ estimation.

1178 The $\gamma + \text{jets}$ control sample

1179 The $Z \rightarrow \nu\bar{\nu} + \text{jets}$ background is also estimated from a $\gamma + \text{jets}$ control sample,
1180 which possesses a larger cross section and kinematic properties similar to those of
1181 $Z \rightarrow \mu\bar{\mu}$ events where the photon is ignored [74][75].

1182 Exactly one photon is selected, satisfying identification criteria as detailed in Table
1183 4.3, with a minimum $p_T > 165$ GeV to satisfy trigger thresholds and $|\eta| < 1.45$ to
1184 ensure the photon remains in the barrel of the detector. The photon is ignored for
1185 the purpose of the calculation of event level variables, and identical selection cuts
1186 to the hadronic signal region are applied.

1187 Additional selection criteria of $\Delta R(\gamma, \text{jet}) < 1.0$, between the photon and all jets is
1188 applied to ensure the acceptance of only well isolated $\gamma + \text{jets}$ events. Given that
1189 the photon is ignored, this control sample can only be applied in the H_T region $>$
1190 375 GeV, due to the trigger thresholds on the minimum p_T of the photon, and the
1191 requirement of an $\alpha_T > 0.55$ cut.

1192 The α_T requirement is relaxed.

₁₁₉₃ **4.3. Trigger Strategy**

₁₁₉₄ **4.4. A method to determine MC yields with higher
statistical precision**

₁₁₉₅ **4.5. Systematic Uncertainties on Transfer Factors**

₁₁₉₆ **4.6. Searches for Natural SUSY with B-tag
templates.**

₁₁₉₇ Btag Templates blah blah

Chapter 5.

¹²⁰⁰ Results

¹²⁰¹ Results at 12fb 8TeV

¹²⁰² 5.1. Statistical Interpretation

¹²⁰³ Likelihood stuff

¹²⁰⁴ 5.2. Interpretation in Simplified Signal Models

¹²⁰⁵ Result interpretation

¹²⁰⁶

Appendix A.

¹²⁰⁷ Miscellaneous

¹²⁰⁸ A.1. Noise Filters

¹²⁰⁹ For Calo jets the following criteria were applied:

¹²¹⁰ • N90 hits > 1 ,

¹²¹¹ • HBHE > 0.01 ,

¹²¹² • fHPD < 0.98 ,

¹²¹³ For PF jets the following criteria were applied:

¹²¹⁴ • Neutral hadron fraction < 0.99 ,

¹²¹⁵ • Neutral EM fraction < 0.99 ,

¹²¹⁶ • Number of constituents > 1 ,

¹²¹⁷ • Charged hadron fraction > 0 ,

¹²¹⁸ • Charged multiplicity > 0 ,

¹²¹⁹ • Charged EM fraction < 0.99 .

¹²²⁰ The following noise filters are applied, to remove events with spurious, non-physical
¹²²¹ jets or missing transverse energy.

¹²²² • CSC tight beam halo filter,

¹²²³ • HBHE noise filter with isolated noise rejection,

- 1224 • HCAL laser filter,
- 1225 • ECAL dead cell trigger primitive (TP) filter,
- 1226 • Tracking failure filter,
- 1227 • Bad EE Supercrystal filter,
- 1228 • ECAL Laser correction filter.

1229 A.2. Primary Vertices

1230 The pileup per event is defined by the number of 'good' reconstructed primary vertices
1231 in the event, with each vertex satisfying the following requirements

- 1232 • $N_{dof} > 4$;
- 1233 • vertex position along the bead direction of $|z_{vtx}| < 24\text{cm}$;
- 1234 • vertex position perpendicular to the beam of $\rho < 2\text{cm}$.

Appendix B.

¹²³⁵ L1 Jets

¹²³⁶ B.1. Jet matching efficiencies

¹²³⁷ The single jet turn-on curves are derived from events independent of whether the leading
¹²³⁸ jet in an event is matched to a Level 1 jet using ΔR matching detailed in Section (3.4.3)
¹²³⁹ or not. These turn-ons are produced from events which are not triggered on jet quantities
¹²⁴⁰ and therefore it is not guaranteed that the lead jet of an event will be seeded by a Level
¹²⁴¹ 1 jet. Figure B.1 shows the particular matching efficiency of a lead jet to a L1 jet.

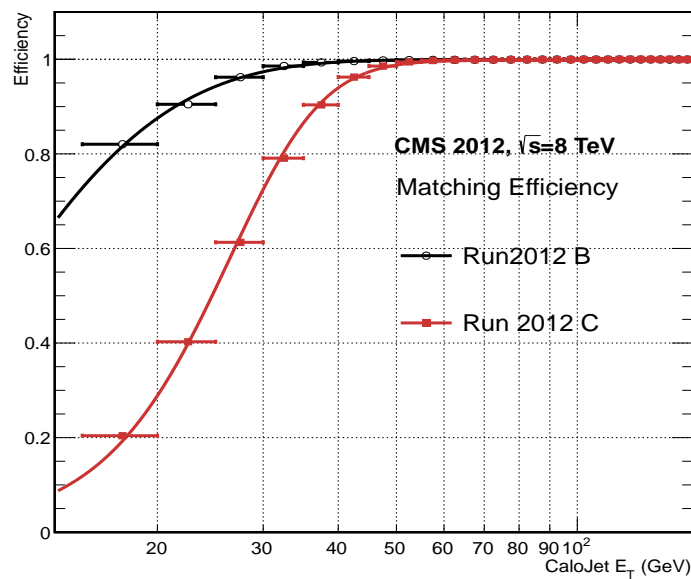


Figure B.1.: Leading jet matching efficiency as a function of the offline CaloJet E_T , measured in an isolated muon triggered dataset in the 2012B and 2012C run periods.

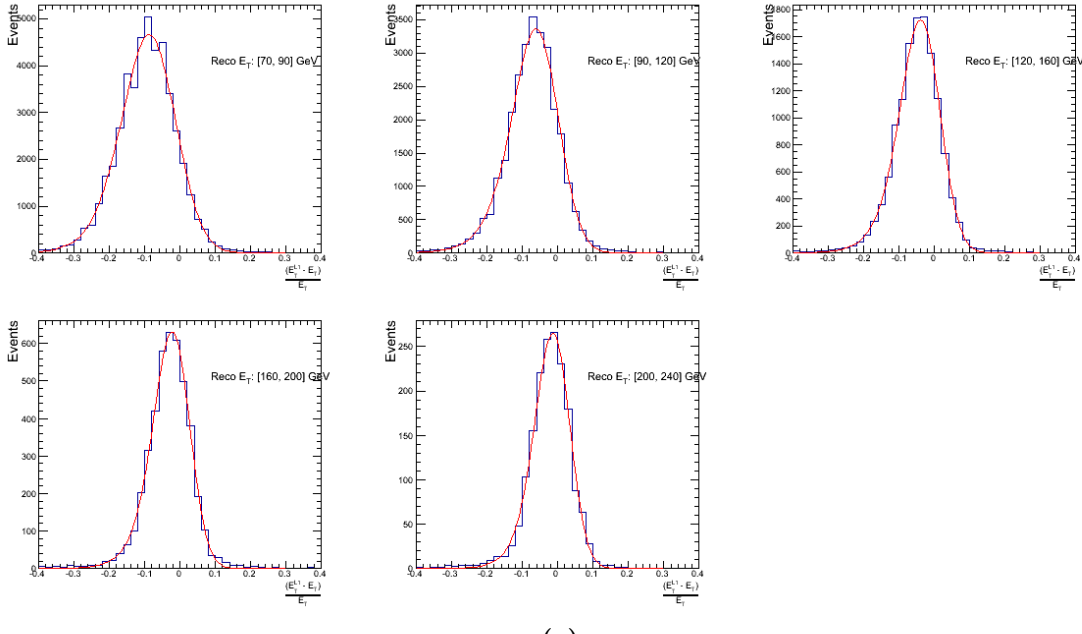
Run Period	μ	σ
2012B	6.62 ± 0.01	0.79 ± 0.03
2012C	19.51 ± 0.03	7.14 ± 0.02

Table B.1.: Results of a cumulative EMG function fit to the turn-on curves for the matching efficiency of the leading jet in an event to a Level-1 jet in run 2012C and 2012B data, measured in an isolated muon triggered sample. The turn-on point, μ , and resolution, σ , are measured with respect to offline Calo Jet E_T .

It can be seen that the turn on is sharper during the 2012B run period. The seed threshold requirement of a 5 GeV jet seed in run 2012C results in more events in which even the lead offline jet does not have an associated L1 jet. For larger jet E_T thresholds, typical of thresholds used in physics analyses, 100% efficiency is observed.

The matching efficiencies have a μ values of 6.62 GeV and 19.51 GeV for Run 2012B and 2012C respectively and is shown in Table B.1.

B.2. Leading Jet Energy Resolution



(a)

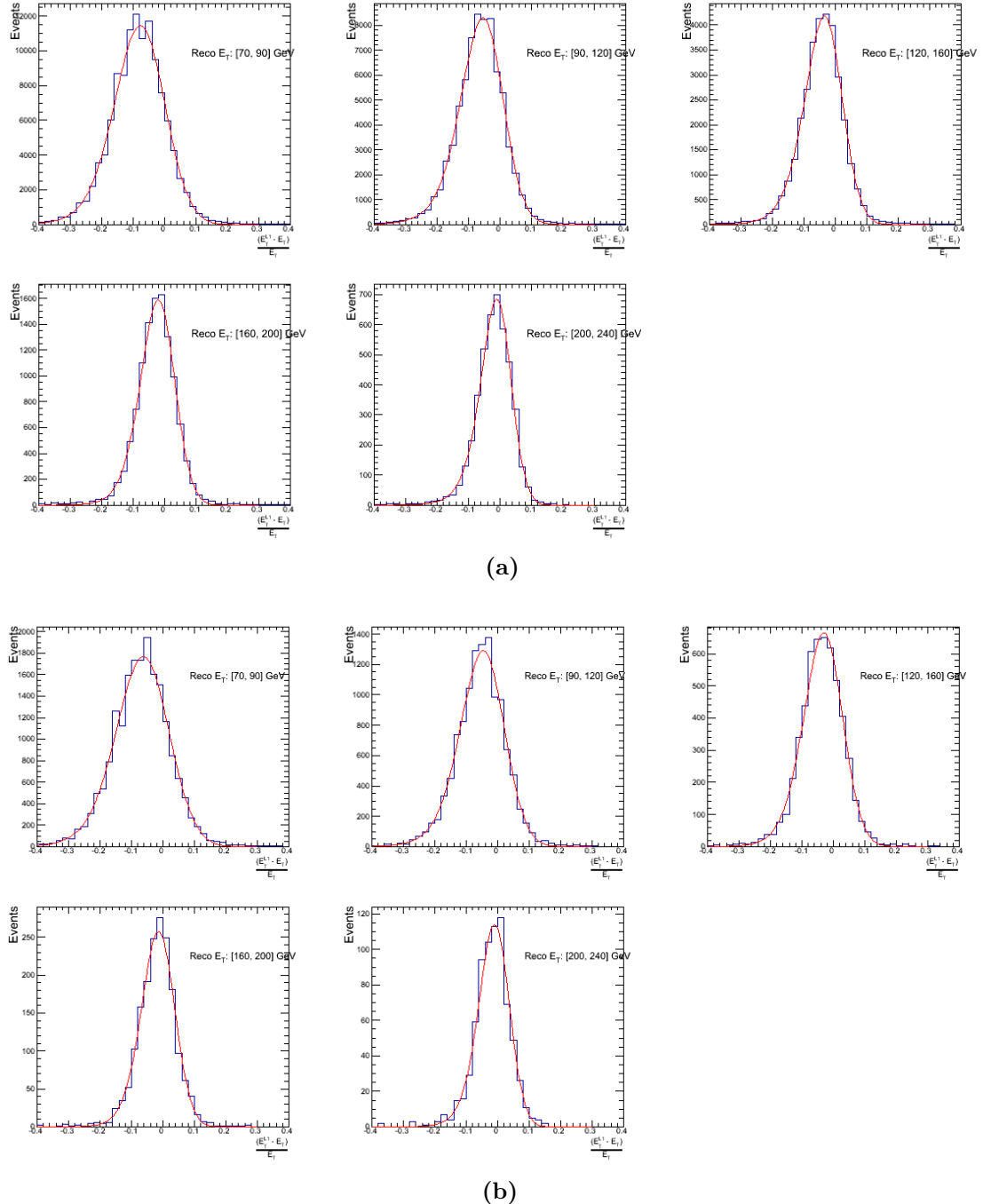
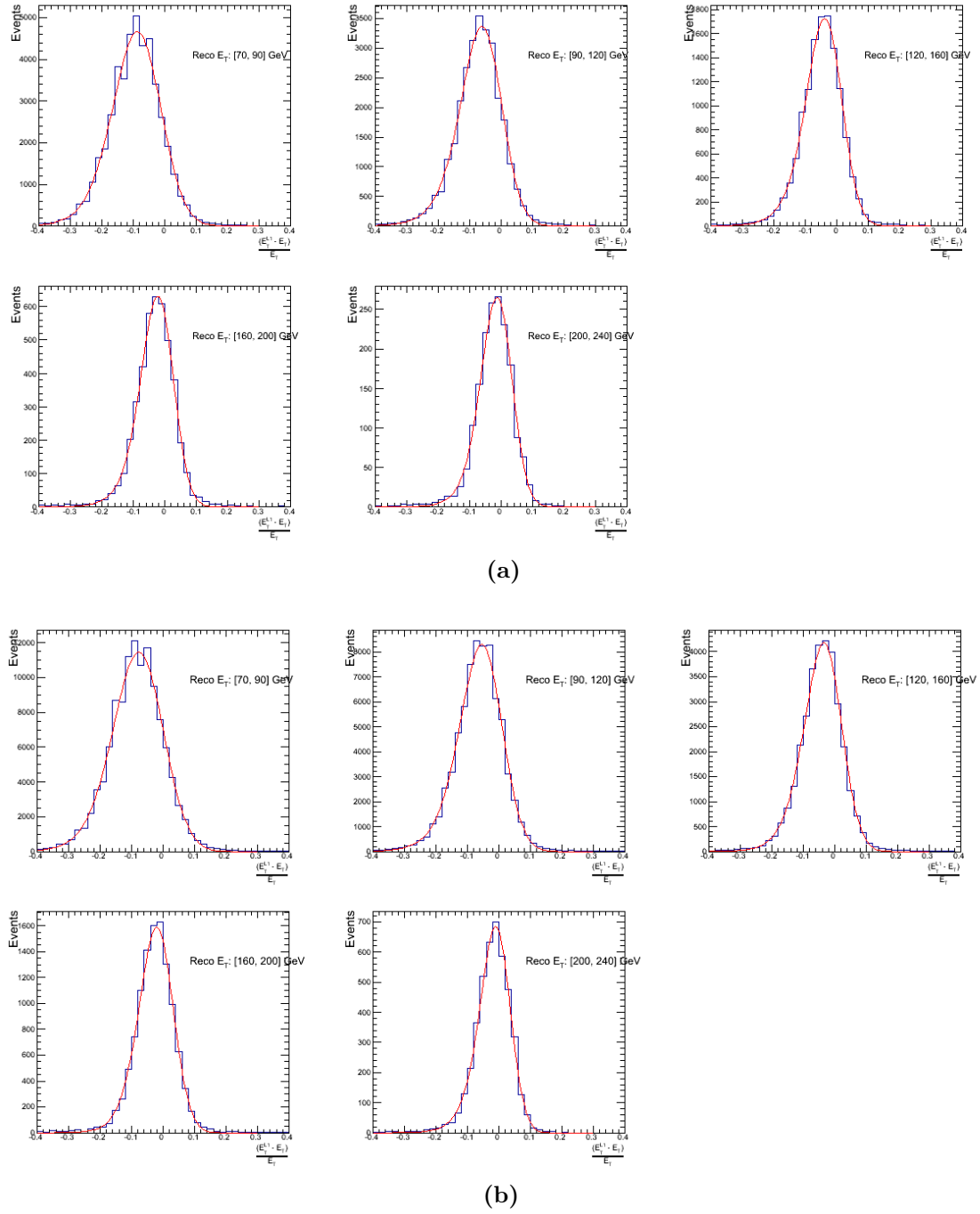


Figure B.2.: Resolution plots of the leading offline jet Calo E_T measured as a function of $\frac{(E_T^{\text{L1}} - E_T^{\text{Offline}})}{E_T^{\text{Offline}}}$ for low (a), medium (b) and high (c) pile-up conditions.



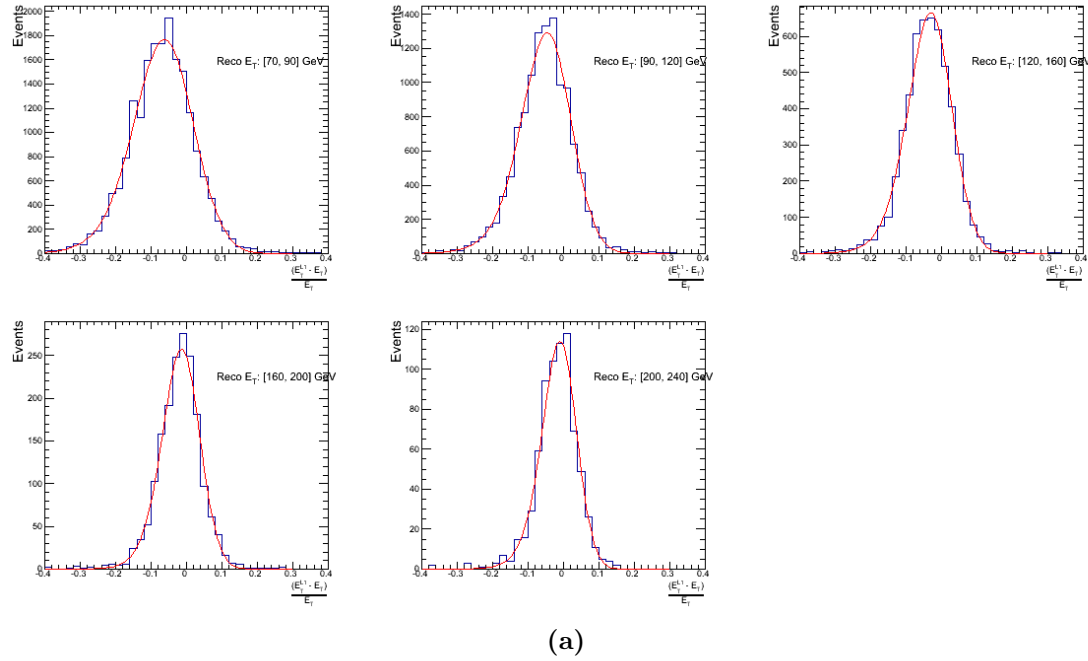


Figure B.3.: Resolution plots of the leading offline jet PF E_T measured as a function of $\frac{(L1 E_T - Offline E_T)}{Offline E_T}$ for low (a), medium (b) and high (c) pile-up conditions.

1249 B.3. Resolution for Energy Sum Quantities

1250 The following plots show the resolution parameters for the four energy sum quantities as
 1251 a function of the quantity (q) itself. In this case, The mean and RMS of the individual
 1252 $\frac{(L1 q - Offline q)}{Offline q}$ distributions, in bins of the quantity q is displayed.

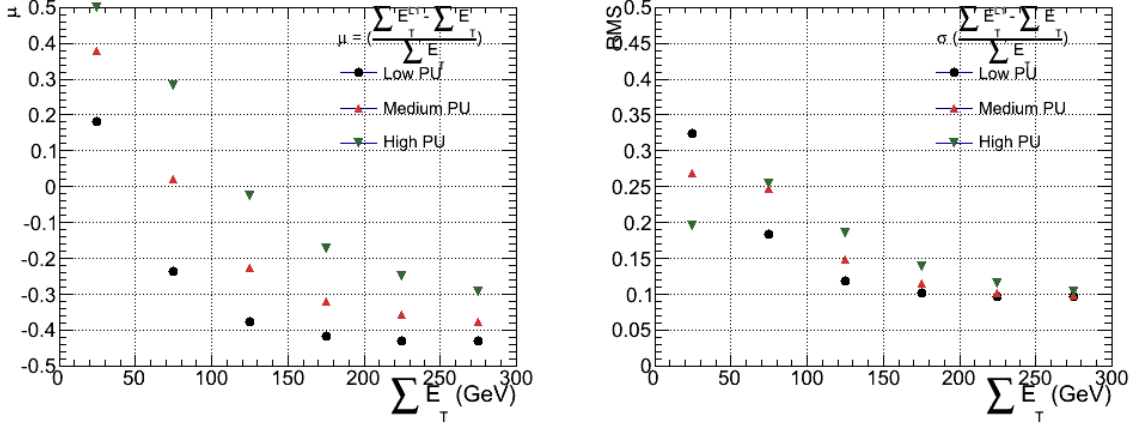


Figure B.4.: $\sum E_T$ resolution parameters in bins of Calo $\sum E_T$ measured for the defined low, medium and high pile up conditions. The plots show the mean μ (left), resolution σ (RMS) of the $\frac{\Delta q}{q}$ distributions.

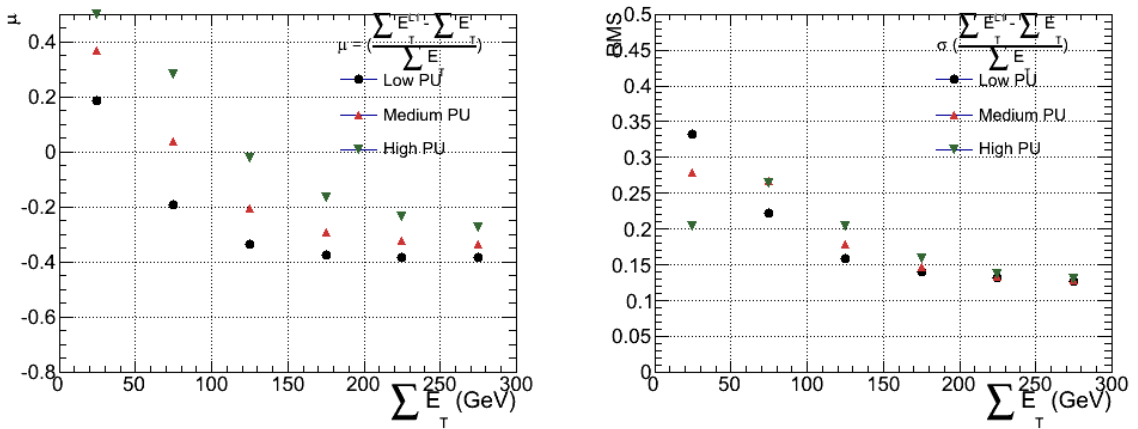


Figure B.5.: $\sum E_T$ resolution parameters in bins of PF $\sum E_T$ measured for the defined low, medium and high pile up conditions. The plots show the mean μ (left), resolution σ (RMS) of the $\frac{\Delta q}{q}$ distributions.

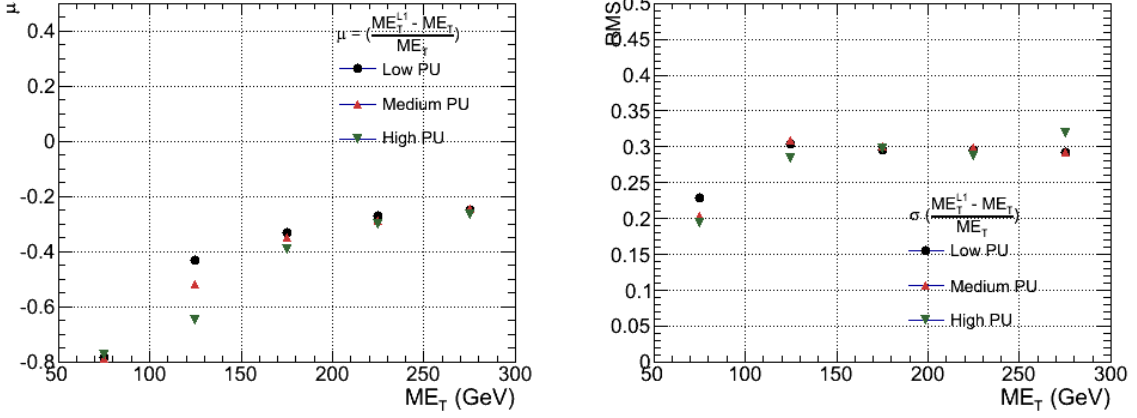


Figure B.6.: \mathcal{E}_T resolution parameters in bins of Calo \mathcal{E}_T measured for the defined low, medium and high pile up conditions. The plots show the mean μ (left), resolution σ (RMS) of the $\frac{\Delta q}{q}$ distributions.

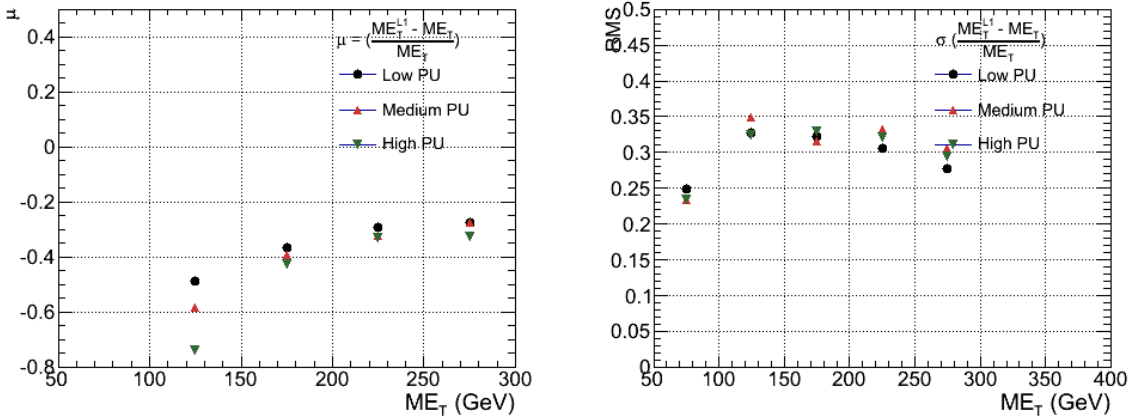


Figure B.7.: \mathcal{E}_T resolution parameters in bins of PF \mathcal{E}_T measured for the defined low, medium and high pile up conditions. The plots show the mean μ (left), resolution σ (RMS) of the $\frac{\Delta q}{q}$ distributions.

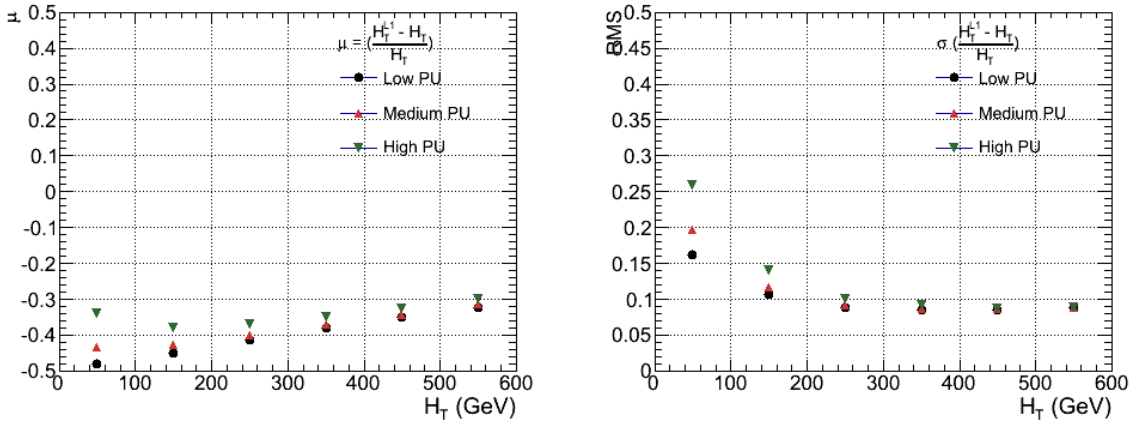


Figure B.8.: H_T resolution parameters in bins of Calo H_T measured for the defined low, medium and high pile up conditions. The plots show the mean μ (left), resolution σ (RMS) of the $\frac{\Delta q}{q}$ distributions.

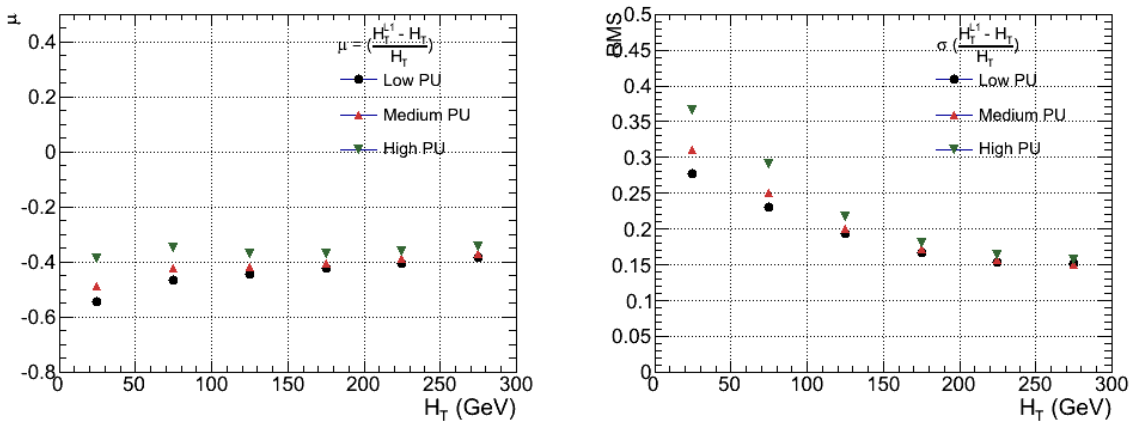


Figure B.9.: H_T resolution parameters in bins of PF H_T measured for the defined low, medium and high pile up conditions. The plots show the mean μ (left), resolution σ (RMS) of the $\frac{\Delta q}{q}$ distributions.

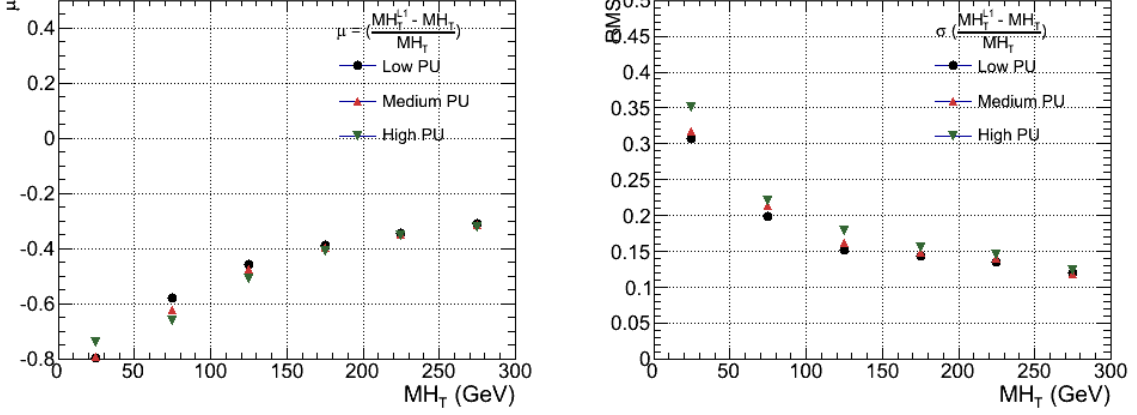


Figure B.10.: H_T resolution parameters in bins of H_T measured for the defined low, medium and high pile up conditions. The plots show the mean μ (left), resolution σ (RMS) of the $\frac{\Delta q}{q}$ distributions.

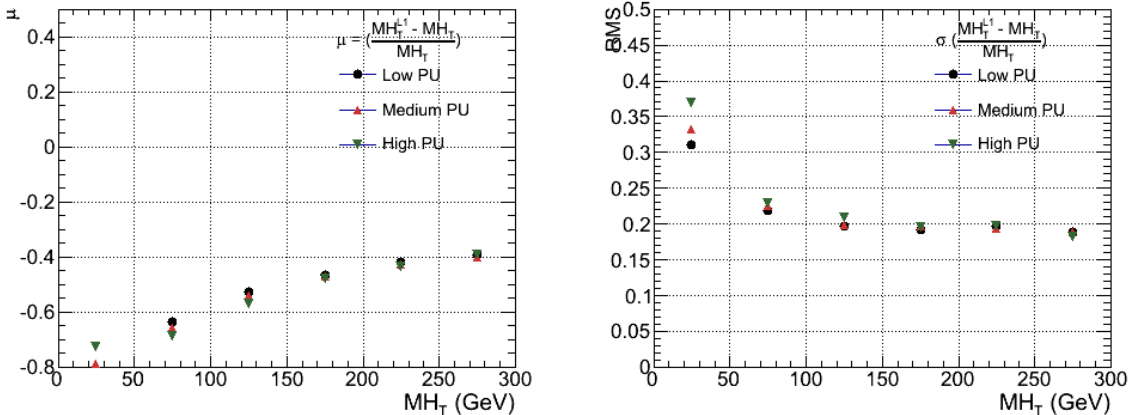


Figure B.11.: H_T resolution parameters in bins of PF H_T measured for the defined low, medium and high pile up conditions. The plots show the mean μ (left), resolution σ (RMS) of the $\frac{\Delta q}{q}$ distributions.

¹²⁵⁴ Bibliography

- ¹²⁵⁵ [1] J. Beringer *et al.*, “Review of Particle Physics (RPP),” *Phys.Rev.*, vol. D86, p. 010001, 2012.
- ¹²⁵⁶ [2] G. H. et al., “Nine-year wilkinson microwave anisotropy probe (wmap) observations: Cosmological parameter results,” *The Astrophysical Journal Supplement Series*, vol. 208, no. 2, p. 19, 2013.
- ¹²⁵⁷ [3] G. Aad *et al.*, “Observation of a new particle in the search for the Standard Model Higgs boson with the ATLAS detector at the LHC,” *Phys.Lett.*, vol. B716, pp. 1–29, 2012.
- ¹²⁵⁸ [4] S. Chatrchyan *et al.*, “Observation of a new boson at a mass of 125 GeV with the CMS experiment at the LHC,” *Phys.Lett.*, vol. B716, pp. 30–61, 2012.
- ¹²⁵⁹ [5] S. Chatrchyan *et al.*, “Search for supersymmetry in hadronic final states with missing transverse energy using the variables AlphaT and b-quark multiplicity in pp collisions at 8 TeV,” *Eur.Phys.J.*, vol. C73, p. 2568, 2013.
- ¹²⁶⁰ [6] S. Weinberg, “A model of leptons,” *Phys. Rev. Lett.*, vol. 19, pp. 1264–1266, Nov 1967.
- ¹²⁶¹ [7] S. Glashow, “Partial Symmetries of Weak Interactions,” *Nucl.Phys.*, vol. 22, pp. 579–588, 1961.
- ¹²⁶² [8] A. Salam, “Weak and Electromagnetic Interactions,” *Conf.Proc.*, vol. C680519, pp. 367–377, 1968.
- ¹²⁶³ [9] G. Hooft, “Renormalizable lagrangians for massive yang-mills fields,” *Nuclear Physics B*, vol. 35, no. 1, pp. 167 – 188, 1971.
- ¹²⁶⁴ [10] F. Hasert *et al.*, “Observation of Neutrino Like Interactions Without Muon Or Electron in the Gargamelle Neutrino Experiment,” *Phys.Lett.*, vol. B46, pp. 138–140, 1973.

- 1279 [11] G. Arnison *et al.*, “Experimental Observation of Lepton Pairs of Invariant Mass
1280 Around 95-GeV/c**2 at the CERN SPS Collider,” *Phys.Lett.*, vol. B126, pp. 398–410,
1281 1983.
- 1282 [12] M. Banner *et al.*, “Observation of Single Isolated Electrons of High Transverse
1283 Momentum in Events with Missing Transverse Energy at the CERN anti-p p
1284 Collider,” *Phys.Lett.*, vol. B122, pp. 476–485, 1983.
- 1285 [13] E. Noether, “Invariante variationsprobleme,” *Nachrichten von der Gesellschaft
1286 der Wissenschaften zu Gttingen, Mathematisch-Physikalische Klasse*, vol. 1918,
1287 pp. 235–257, 1918.
- 1288 [14] F. Halzen and A. D. Martin, “Quarks and leptons.” Wiley, 1985.
- 1289 [15] *Introduction to Elementary Particles*. Wiley-VCH, 2nd ed., Oct. 2008.
- 1290 [16] C. S. Wu, E. Ambler, R. W. Hayward, D. D. Hoppes, and R. P. Hudson, “Ex-
1291 perimental Test of Parity Conservation in Beta Decay,” *Physical Review*, vol. 105,
1292 pp. 1413–1415, Feb. 1957.
- 1293 [17] P. Higgs, “Broken symmetries, massless particles and gauge fields,” *Physics Letters*,
1294 vol. 12, no. 2, pp. 132 – 133, 1964.
- 1295 [18] F. Englert and R. Brout, “Broken symmetry and the mass of gauge vector mesons,”
1296 *Phys. Rev. Lett.*, vol. 13, pp. 321–323, Aug 1964.
- 1297 [19] P. W. Higgs, “Broken symmetries and the masses of gauge bosons,” *Phys. Rev. Lett.*,
1298 vol. 13, pp. 508–509, Oct 1964.
- 1299 [20] G. S. Guralnik, C. R. Hagen, and T. W. B. Kibble, “Global conservation laws and
1300 massless particles,” *Phys. Rev. Lett.*, vol. 13, pp. 585–587, Nov 1964.
- 1301 [21] S. Weinberg, “A model of leptons,” *Phys. Rev. Lett.*, vol. 19, pp. 1264–1266, Nov
1302 1967.
- 1303 [22] H. Yukawa, “On the interaction of elementary particles. i,” *Progress of Theoretical
1304 Physics Supplement*, vol. 1, pp. 1–10, 1955.
- 1305 [23] Y. e. a. Fukuda, “Evidence for oscillation of atmospheric neutrinos,” *Phys. Rev.
1306 Lett.*, vol. 81, pp. 1562–1567, Aug 1998.
- 1307 [24] R. Becker-Szendy, C. Bratton, D. Casper, S. Dye, W. Gajewski, *et al.*, “A Search
1308 for muon-neutrino oscillations with the IMB detector,” *Phys.Rev.Lett.*, vol. 69,

- 1309 pp. 1010–1013, 1992.
- 1310 [25] S. P. Martin, “A Supersymmetry primer,” 1997.
- 1311 [26] H. Nilles, *Supersymmetry, Supergravity and Particle Physics*. Physics reports, North-Holland Physics Publ., 1984.
- 1312
- 1313 [27] H. E. Haber and G. L. Kane, “The Search for Supersymmetry: Probing Physics Beyond the Standard Model,” *Phys.Rept.*, vol. 117, pp. 75–263, 1985.
- 1314
- 1315 [28] E. Witten, “Dynamical Breaking of Supersymmetry,” *Nucl.Phys.*, vol. B188, p. 513, 1981.
- 1316
- 1317 [29] J. Wess and B. Zumino, “Supergauge transformations in four dimensions,” *Nuclear Physics B*, vol. 70, no. 1, pp. 39 – 50, 1974.
- 1318
- 1319 [30] H. Muller-Kirsten and A. Wiedemann, *Introduction to Supersymmetry*. World Scientific lecture notes in physics, World Scientific, 2010.
- 1320
- 1321 [31] I. Aitchison, *Supersymmetry in Particle Physics: An Elementary Introduction*. Cambridge University Press, 2007.
- 1322
- 1323 [32] K. A. Intriligator and N. Seiberg, “Lectures on Supersymmetry Breaking,” *Class.Quant.Grav.*, vol. 24, pp. S741–S772, 2007.
- 1324
- 1325 [33] Y. Shadmi, “Supersymmetry breaking,” pp. 147–180, 2006.
- 1326
- 1327 [34] C. Burgess, P. G. Camara, S. de Alwis, S. Giddings, A. Maharana, *et al.*, “Warped Supersymmetry Breaking,” *JHEP*, vol. 0804, p. 053, 2008.
- 1328
- 1329 [35] H. Murayama, “Supersymmetry breaking made easy, viable, and generic,” 2007.
- 1330
- 1331 [36] H. Baer and X. Tata, *Weak Scale Supersymmetry: From Superfields to Scattering Events*. Cambridge University Press, 2006.
- 1332
- 1333 [37] S. P. Martin, “Implications of supersymmetric models with natural r-parity conservation,” 1996.
- 1334
- 1335 [38] G. L. Kane, C. F. Kolda, L. Roszkowski, and J. D. Wells, “Study of constrained minimal supersymmetry,” *Phys.Rev.*, vol. D49, pp. 6173–6210, 1994.
- 1336
- 1337 [39] C. Stlege, G. Bertone, D. Cerdeno, M. Fornasa, R. Ruiz de Austri, *et al.*, “Updated global fits of the cmSSM including the latest LHC SUSY and Higgs searches and XENON100 data,” *JCAP*, vol. 1203, p. 030, 2012.

- 1338 [40] M. Citron, J. Ellis, F. Luo, J. Marrouche, K. Olive, *et al.*, “The End of the CMSSM
1339 Coannihilation Strip is Nigh,” *Phys.Rev.*, vol. D87, p. 036012, 2013.
- 1340 [41] D. Ghosh, M. Guchait, S. Raychaudhuri, and D. Sengupta, “How Constrained is
1341 the cMSSM?,” *Phys.Rev.*, vol. D86, p. 055007, 2012.
- 1342 [42] D. Alves *et al.*, “Simplified Models for LHC New Physics Searches,” *J.Phys.*, vol. G39,
1343 p. 105005, 2012.
- 1344 [43] J. Alwall, P. Schuster, and N. Toro, “Simplified Models for a First Characterization
1345 of New Physics at the LHC,” *Phys.Rev.*, vol. D79, p. 075020, 2009.
- 1346 [44] S. Chatrchyan *et al.*, “Interpretation of Searches for Supersymmetry with simplified
1347 Models,” *Phys.Rev.*, vol. D88, p. 052017, 2013.
- 1348 [45] J. Hisano, K. Kurosawa, and Y. Nomura, “Natural effective supersymmetry,”
1349 *Nucl.Phys.*, vol. B584, pp. 3–45, 2000.
- 1350 [46] M. Papucci, J. T. Ruderman, and A. Weiler, “Natural SUSY Endures,” *JHEP*,
1351 vol. 1209, p. 035, 2012.
- 1352 [47] B. Allanach and B. Gripaios, “Hide and Seek With Natural Supersymmetry at the
1353 LHC,” *JHEP*, vol. 1205, p. 062, 2012.
- 1354 [48] K. Aamodt *et al.*, “The ALICE experiment at the CERN LHC,” *JINST*, vol. 3,
1355 p. S08002, 2008.
- 1356 [49] G. Aad *et al.*, “The ATLAS Experiment at the CERN Large Hadron Collider,”
1357 *JINST*, vol. 3, 2008.
- 1358 [50] R. Adolphi *et al.*, “The cms experiment at the cern lhc,” *JINST*, vol. 0803, p. S08004,
1359 2008.
- 1360 [51] A. A. Alves *et al.*, “The LHCb Detector at the LHC,” *JINST*, vol. 3, p. S08005,
1361 2008.
- 1362 [52] J.-L. Caron, “Lhc layout.. schema general du lhc..” Sep 1997.
- 1363 [53] C. Collaboration, “Cms luminosity - public results.”
1364 twiki.cern.ch/twiki/bin/view/CMSPublic/LumiPublicResults., 2011.
- 1365 [54] CERN, “Cms compact muon solenoid..” <http://public.web.cern.ch/public/Objects/LHC/CMSnc.jpg>
1366 Feb 2010.

- 1367 [55] *The CMS electromagnetic calorimeter project: Technical Design Report*. Technical
1368 Design Report CMS, Geneva: CERN, 1997.
- 1369 [56] *The CMS muon project: Technical Design Report*. Technical Design Report CMS,
1370 Geneva: CERN, 1997.
- 1371 [57] CMS Collaboration, “The cms physics technical design report, volume 1,”
1372 *CERN/LHCC*, vol. 2006-001, 2006.
- 1373 [58] M. Cacciari, G. P. Salam, and G. Soyez, “The anti- k_t jet clustering algorithm,”
1374 *Journal of High Energy Physics*, vol. 2008, no. 04, p. 063, 2008.
- 1375 [59] “Jet performance in pp collisions at 7 tev,” Tech. Rep. CMS-PAS-JME-10-003,
1376 CERN, Geneva, 2010.
- 1377 [60] X. Janssen, “Underlying event and jet reconstruction in cms,” Tech. Rep. CMS-CR-
1378 2011-012, CERN, Geneva, Jan 2011.
- 1379 [61] T. C. collaboration, “Determination of jet energy calibration and transverse mo-
1380 mentum resolution in cms,” *Journal of Instrumentation*, vol. 6, no. 11, p. P11002,
1381 2011.
- 1382 [62] R. Eusebi and on behalf of the CMS collaboration), “Jet energy corrections and
1383 uncertainties in cms: reducing their impact on physics measurements,” *Journal of
1384 Physics: Conference Series*, vol. 404, no. 1, p. 012014, 2012.
- 1385 [63] “Algorithms for b Jet identification in CMS,” Tech. Rep. CMS-PAS-BTV-09-001,
1386 CERN, 2009. Geneva, Jul 2009.
- 1387 [64] “Performance of b tagging at $\sqrt{s}=8$ tev in multijet, ttbar and boosted topology
1388 events,” no. CMS-PAS-BTV-13-001, 2013.
- 1389 [65] T. C. collaboration, “Identification of b-quark jets with the cms experiment,” *Journal
1390 of Instrumentation*, vol. 8, no. 04, p. P04013, 2013.
- 1391 [66] S. Dasu *et al.*, “CMS. The TriDAS project. Technical design report, vol. 1: The
1392 trigger systems,” 2000.
- 1393 [67] P. Sphicas, “CMS: The TriDAS project. Technical design report, Vol. 2: Data
1394 acquisition and high-level trigger,” 2002.
- 1395 [68] J. B. et al., “Calibration and Performance of the Jets and Energy Sums in the
1396 Level-1 Trigger ,” no. CMS IN 2013/006 (2013), 2013.

- 1397 [69] B. et al., “Study of Level-1 Trigger Jet Performance in High Pile-up Running
1398 Conditions,” no. CMS IN 2013/007 (2013), 2013.
- 1399 [70] J. J. Brooke, “Performance of the cms level-1 trigger,” Tech. Rep. CMS-CR-2012-322.
1400 CERN-CMS-CR-2012-322, CERN, Geneva, Nov 2012.
- 1401 [71] L. Randall and D. Tucker-Smith, “Dijet searches for supersymmetry at the large
1402 hadron collider,” *Phys. Rev. Lett.*, vol. 101, p. 221803, Nov 2008.
- 1403 [72] “SUSY searches with dijet events,” 2008.
- 1404 [73] “Search strategy for exclusive multi-jet events from supersymmetry at CMS,” Tech.
1405 Rep. CMS-PAS-SUS-09-001, CERN, 2009. Geneva, Jul 2009.
- 1406 [74] Z. Bern, G. Diana, L. J. Dixon, F. Febres Cordero, S. Hoche, H. Ita, D. A. Kosower,
1407 D. Maitre, and K. J. Ozeren, “Driving missing data at next-to-leading order,” *Phys.
Rev. D*, vol. 84, p. 114002, Dec 2011.
- 1408 [75] “Data-Driven Estimation of the Invisible Z Background to the SUSY MET Plus
1409 Jets Search,” Tech. Rep. CMS-PAS-SUS-08-002, CERN, 2009. Geneva, Jan 2009.

1411 Acronyms

1412 ALICE	A Large Ion Collider Experiment
1413 ATLAS	A Toroidal LHC ApparatuS
1414 APD	Avalanche Photo-Diodes
1415 BSM	Beyond Standard Model
1416 CERN	European Organization for Nuclear Research
1417 CMS	Compact Muon Solenoid
1418 CMSSM	Compressed Minimal SuperSymmetric Model
1419 CSC	Cathode Stripe Chamber
1420 CSV	Combined Secondary Vertex
1421 CSVM	Combined Secondary Vertex Medium Working Point
1422 DT	Drift Tube
1423 ECAL	Electromagnetic CALorimeter
1424 EB	Electromagnetic CALorimeter Barrel
1425 EE	Electromagnetic CALorimeter Endcap
1426 ES	Electromagnetic CALorimeter pre-Shower
1427 EMG	Exponentially Modified Gaussian
1428 EPJC	European Physical Journal C
1429 EWK	Electroweak Sector
1430 GCT	Global Calorimeter Trigger
1431 GMT	Global MuonTrigger
1432 GT	Global Trigger
1433 HB	Hadron Barrel
1434 HE	Hadron Endcaps

1435	HF	Hadron Forward
1436	HO	Hadron Outer
1437	HCAL	Hadronic CALorimeter
1438	HLT	Higher Level Trigger
1439	LUT	Look Up Table
1440	L1	Level 1 Trigger
1441	LHC	Large Hadron Collider
1442	LHCb	Large Hadron Collider Beauty
1443	LSP	Lightest Supersymmetric Partner
1444	PS	Proton Synchrotron
1445	QED	Quantum Electro-Dynamics
1446	QCD	Quantum Chromo-Dynamics
1447	QFT	Quantum Field Theory
1448	RPC	Resistive Plate Chamber
1449	RCT	Regional Calorimeter Trigger
1450	RMT	Regional Muon Trigger
1451	SUSY	SUperSYmmetry
1452	SM	Standard Model
1453	SMS	Simplified Model Spectra
1454	SPS	Super Proton Synchrotron
1455	TF	Transfer Factor
1456	VEV	Vacuum Expectation Value
1457	VPT	Vacuum Photo-Triodes
1458	WIMP	Weakly Interacting Massive Particle